Tectonics

RESEARCH ARTICLE
10.1029/2019TC005635

Key Points:
- Initiation of the Rio Grande rift appears to be synchronous ~25 Ma and does not support a northward propagation model
- Extension is accommodated by faulting in the northern and southern Rio Grande rift and by magmatic injection in the central Rio Grande rift
- Different rift accommodation mechanisms may be controlled by preexisting weaknesses and lithospheric properties (i.e., thickness)

Supporting Information:
- Supporting Information S1

Correspondence to:
A. L. Abbey,
alabbey@berkeley.edu

Citation:
Abbey, A. L., & Niemi, N. A. (2020). Perspectives on continental rifting processes from spatiotemporal patterns of faulting and magmatism in the Rio Grande rift, USA. *Tectonics*, *39*, e2019TC005635. https://doi.org/10.1029/2019TC005635

Received 26 APR 2019
Accepted 21 NOV 2019
Accepted article online 11 DEC 2019

Perspectives on Continental Rifting Processes From Spatiotemporal Patterns of Faulting and Magmatism in the Rio Grande Rift, USA

Alyssa L. Abbey[1,2] and Nathan A. Niemi[1]

[1]Department of Earth and Environmental Sciences, University of Michigan, Ann Arbor, MI, USA, [2]Now at Department of Earth and Planetary Science, University of California & Berkeley Geochronology Center, Berkeley, CA, USA

Abstract Analysis of spatiotemporal patterns of faulting and magmatism in the Rio Grande rift (RGR) in New Mexico and Colorado, USA, yields insights into continental rift processes, extension accommodation mechanisms, and rift evolution models. We combine new apatite (U-Th-Sm)/He and zircon (U-Th)/He thermochronometric data with previously published thermochronometric data to assess the timing of fault initiation, magnitudes of fault exhumation, and growth and linkage patterns of rift faults. Thermal history modeling of these data reveals contemporaneous rift initiation at ca. 25 Ma in both the northern and southern RGR with continued fault initiation, growth, and linkage progressing from ca. 25 to ca. 15 Ma. The central RGR, however, shows no evidence of Cenozoic fault-related exhumation as observed with thermochronometry and instead reveals extension accommodated through Late Cenozoic magmatic injection. Furthermore, faulting in the northern and southern RGR occurs along an approximately north-south strike, whereas magmatism in the central RGR occurs along the northeast to southwest trending Jemez lineament. Differences in deformation orientation and rift accommodation along strike appear to be related to crustal and lithospheric properties, suggesting that rift structure and geometry are at least partly controlled by inherited lithospheric-scale architecture. We propose an evolutionary model for the RGR that involves initiation of fault-accommodated extension by oblique strain followed by block rotation of the Colorado Plateau, where extension in the RGR is accommodated by faulting (southern and northern RGR) and magmatism (central RGR). This study highlights different processes related to initiation, geometry, extension accommodation, and overall development of continental rifts.

Plain Language Summary We identify patterns of faulting and volcanism in the Rio Grande rift (RGR) in the western United States to better understand how continental rifts evolve. Using methods for documenting rock cooling ages (thermochronology), we determined that rifting began around 25 million years ago (Ma) in both the northern and southern RGR. Rift faults continued to develop and grow for another 10 to 15 million years. The central RGR, however, shows that rift extension occurred through volcanic activity both as eruptions at the surface and as magma injection below the surface since ~15 Ma. Interestingly, RGR faulting in the north and south parts of the rift occurs on a north-south line, while volcanism in the central RGR is along a northeast to southwest line. The differences in the location and orientation of faulting and volcanic activity may be related to the thickness of the lithosphere beneath different parts of the rift. Using these patterns of faulting and magmatism, we propose the RGR evolved through a combination of (1) oblique strain—extension diagonal to the rift and (2) block rotation—where the Colorado Plateau is the rotating block. This detailed study highlights different processes related to the accommodation of extension and the overall development of continental rifts.

1. Introduction

Continental rifting may eventually lead to tectonic plate breakup, an essential part of the tectonic cycle, and yet, the processes that accompany rift initiation, define rift geometry or fault style, control the location of extension, and govern differences in rift extension accommodation mechanisms remain unclear (Nelson et al., 1992). Ultimately, continental rifting is caused by interactions between mantle flow and plate movements; accordingly, extension accommodation, rates of rift development, and fault growth are controlled by combinations of heat transfer, lithospheric structure, far-field stresses, mantle flow, and magmatism (Lavecchia et al., 2017). Additionally, the mechanisms that accommodate extension may be controlled by

crustal and lithospheric properties such as strength, thickness, preexisting weakness, inherited structure, composition, and/or rates of extension (e.g., Brun, 1999; Buck, 1991; Corti, 2012; Fletcher et al., 2018). As such, there are numerous expressions of rifting, for example, rifts can be wide, narrow, magma dominated, have large basin-bounding faults, numerous intrabasin faults, or en echelon geometries (e.g., Brune et al., 2017; Ebinger, 1989; Ebinger et al., 1984; McClay et al., 2002; Molnar et al., 2017; Nelson et al., 1992), emphasizing the roles that faulting and magmatism can have on the geometry and extension accommodation of a rift system (Figure 1; e.g., Buck, 2004; Ebinger, 2005; Buck, 2006; Corti, 2009).

Continental rift systems grow initially as separate basins dominated by the initiation and linkage of individual fault segments (e.g., Abbey & Niemi, 2018; Contreras et al., 2000; Corti, 2008; Ebinger, 2005; McClay et al., 2002; Morley, 1988; Morley et al., 1990; Nelson et al., 1992). Continued growth of separate rift basins via fault tip propagation and segment linkage leads to these basins merging and connecting with each other through what are generically termed *accommodation zones* (ACZs; e.g., Morley, 1988; Ebinger, 1989; Morley et al., 1990; Nelson et al., 1992; Chapin & Cather, 1994; Lewis & Baldridge, 1994; Mack & Seager, 1995; McClay et al., 2002). Such ACZs promote basin integration through strain transfer between and across faults, often facilitating magmatic activity that further aids in strain transferal (e.g., Lewis & Baldridge, 1994; Muirhead et al., 2015; Muirhead et al., 2016; Rowland et al., 2010).

Understanding the spatiotemporal relationships between faulting and magmatism will assist in distinguishing between processes of rift development (e.g., basin growth and linkage and/or hot spot migration; Figure 1) and controls on rift geometry and extension accommodation (e.g., inherited structure or lithospheric architecture). These new insights about rift initiation and development will be helpful for determining the processes and factors controlling the evolution of continental rift systems around the world where there is less available data or more limited access.

Rift initiation and fault growth style (e.g., tip propagation, segment linkage, or constant length with increasing displacement; Kim & Sanderson, 2005) can be well documented in the Rio Grande rift (RGR) in the western United States (Figure 2). The entire rift system is exposed on land, and a plethora of published data related to fault motion, basin sedimentation, volcanism, lithospheric structure, and regional strain rates provides a thorough framework necessary for establishing relationships between faulting, magmatism, and lithospheric structure (Table 1). Moreover, extension in the RGR is relatively slow (Golombek et al., 1983; Kreemer et al., 2010; Liu et al., 2019; Muirhead et al., 2016; Nixon et al., 2016; Savage et al., 1990; Shirvell et al., 2009; van Wijk et al., 2018; Woodward, 1977), which affords the opportunity to capture discrete details about fault growth and rift basin linkage that might otherwise be difficult to detect in more developed rifts and/or more rapidly evolving extensional systems (e.g., Ethiopian rift and Gulf of California).

Here we review existing interpretations and controversies about the evolution of the RGR and summarize the physiographic characteristics, which have influenced many of the contradicting explanations about RGR development. We then synthesize all of the published low-temperature thermochronometry data available along the RGR to elucidate spatial patterns of rift-flank fault initiation, growth, and linkage (Figures 3–5). Supplementing these data, we present new thermochronometric samples and analyses designed to constrain the total magnitude of rift-related extension (typically ZHe) or to refine the uncertainty on the initiation of faulting (typically AHe) (Table 2). Using inverse thermal history modeling on these data assembled into vertical transects (combining the compiled published data with our new data), we obtain initiation timing and magnitudes and rates of exhumation along the rift-flank faults of the RGR. Finally, we assess compositional and spatiotemporal patterns in magmatism to further identify and constrain processes of rift basin linkage and extension accommodation.

2. RGR Controversy

Aspects related to the temporal growth of the RGR are highly disputed, with debate centering around two main hypotheses.

1. Extension began in the southern part of the rift and propagated northward over time so that the basins in the northern RGR are the youngest in the rift system (Duller et al., 2012; Frankel & Pazzaglia, 2006; Heller et al., 2003; Leonard, 2002; McMillan et al., 2002). Rift growth via propagation gains support from general models involving propagating faults that connect through preexisting weak zones or migration of

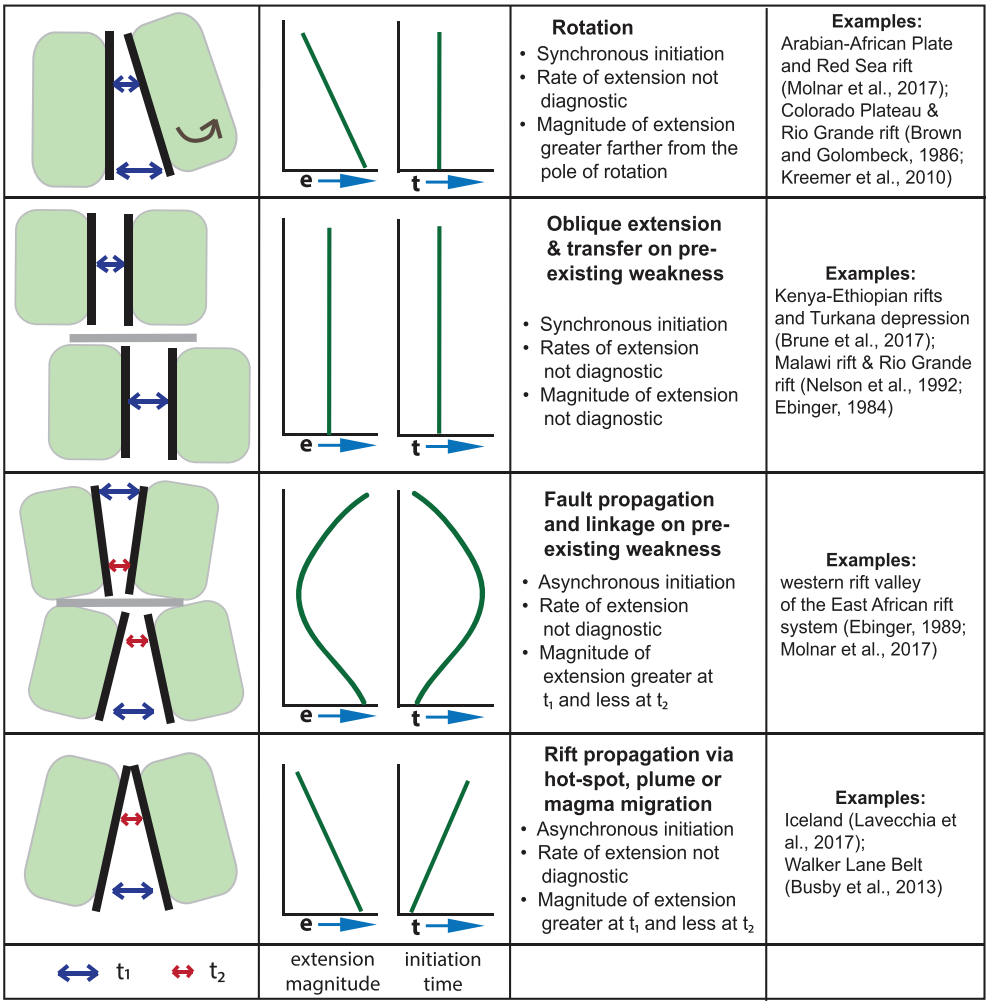

Figure 1. Generalized models of continental rifting. Each model has diagnostic characteristicsin the timing of initiation, rate of extension, and magnitude of extension (middle columns), whichcan be used to differentiate between possible rift models. Second column from the left shows thedifferences in the magnitudes of extension and timing of rift initiation for each model. e = extension magnitude increasing to the right, t = initiation timing, younger initiation to the right.

magma (Figure 1). Within the RGR, far-field tilting of Miocene sediments, increased sedimentation in the Great Plains, and the existence of young (<6 Ma) mafic volcanism and seismic activity in northern Colorado have been invoked as evidence for a northward propagation model (Cosca et al., 2014; Duller et al., 2012; Heller et al., 2003; Kellogg, 1999; Leonard, 2002; Leonard et al., 2002; McMillan et al., 2002; Naeser et al., 2002; Nakai et al., 2017).

2. Rifting was primarily synchronous along the length of the RGR (Chapin & Cather, 1994; Landman & Flowers, 2013; Ricketts et al., 2016). Typical models supporting synchronous rifting include either block rotation or oblique strain (Figure 1; Ebinger et al., 1984; Brown & Golombek, 1986; Ebinger, 1989; Nelson et al., 1992; McClay et al., 2002; Kreemer et al., 2010; Busby, 2013; Molnar et al., 2017; Lavecchia et al., 2017; Brune et al., 2017). Additionally, interbasin synrift sedimentation and thermochronometry data from the rift flanks have been invoked to support a model of synchronous rift initiation (Chapin & Cather, 1994; Ingersoll, 2001; Landman & Flowers, 2013; Ricketts et al., 2015).

However, synrift strata and basin subsidence in individual basins of the RGR often have poor age resolution (Baldridge et al., 1994; van Alstine, 1969; Van Alstine & Lewis, 1960; van Wijk et al., 2018; Zhu & Fan, 2018), and rift-related magmatism is sparse in many RGR basins (Cosca et al., 2014; McMillan et al., 2000). Additionally, regional tilting or distal erosion and sedimentation are indirect proxies for rift activity, hampered by a deficiency of coherent detail along the entire length of the rift and potentially being ascribable

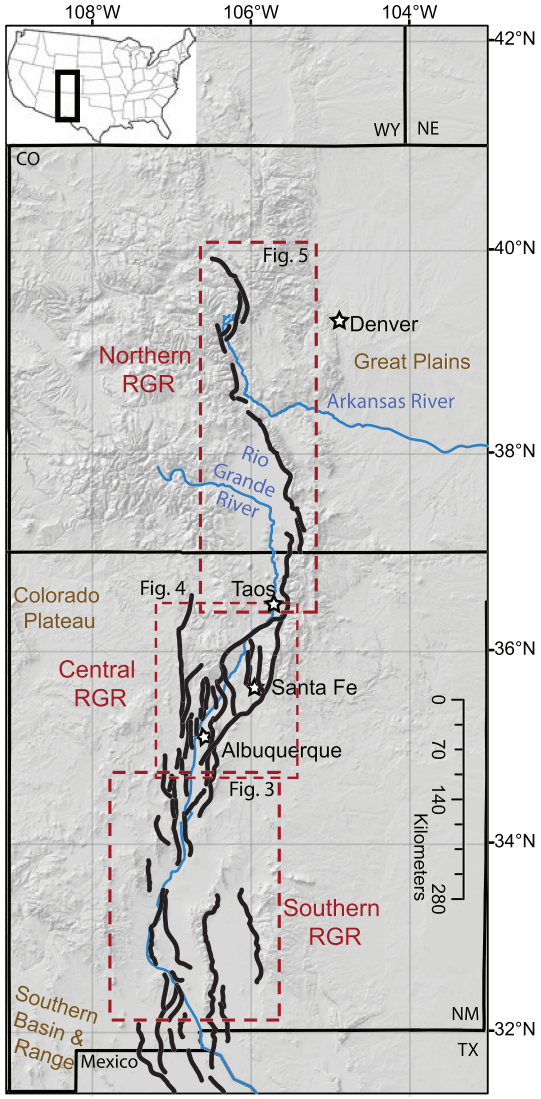

Figure 2. Location of the Rio Grande rift (RGR) in New Mexico and Colorado. Simplified Quaternary faults (bold black lines; Machette et al., 1998). Dashed red outlines mark the regions we define as the northern, central, and southern RGR.

to nontectonic processes (e.g., climate; van Wijk et al., 2018). Therefore, we lack a set of criteria by which we can reliably distinguish between rift models proposed for the development of the entire RGR system.

2.1. Approach to Resolving Spatial and Temporal Patterns of Faulting and Magmatism in the RGR

Fault segment growth and linkage can be observed and quantified with low-temperature thermochronometry analyses in vertical transects collected on exhuming normal fault blocks (Abbey & Niemi, 2018; Boone et al., 2019; Curry et al., 2016; Stockli et al., 2000; Stockli et al., 2002). Low-temperature thermochronometers are powerful tools for understanding near-surface (1–7 km) thermal histories of the crust and thus are sensitive to processes that affect the upper crust, including erosion and faulting. Low-temperature thermochronometry can be used throughout the RGR to constrain timing, rates, and magnitudes of faulting as these approaches are sensitive to temperature ranges from ~30 to ~230 °C depending on mineral system and radiation damage—apatite (U-Th-Sm)/He (AHe): ~30 and 90 °C; apatite fission track (AFT): ~70 and 150 °C; and zircon (U-Th)/He (ZHe): ~130 to ~230 °C (Ehlers, 2005; Farley, 2002; Flowers et al., 2009; Guenthner et al., 2013; Kelley & Chapin, 1995; Reiners, 2005; Reiners et al., 2002; Shuster et al., 2006).

We compile AHe, ZHe, and AFT data from 15 studies amounting to over 400 low-temperature thermochronometry ages that span >800 km along-strike of the RGR (Table 1 and Figures 3–5). We analyze the spatial distribution of these data and extract sample suites, which we consider to have spatial relationships consistent with a vertical sampling transect. We define a vertical transect as including at least three thermochronometric samples that are within 5 km of the fault trace at the surface. We targeted places where >500 m was traversed in vertical space across <5 km of horizontal space to ensure a high-relief relationship between the samples. We identified one to four groups of samples that fit our criteria for a vertical transect in each RGR basin with the exception of the three southernmost basins, (Palomas, Jornada, and Tularosa basins) where there were no such spatial relationships in the published samples (Figures 3–5 and Table 3).

In total, we identified 14 groups of samples that fit our criteria for a vertical transect (Figures 3–5 and Table 3). Many of these transects are composed of samples from multiple studies, while in other cases, samples may have been originally collected in a vertical transect but had not previously been modeled as such. Applying modern thermal history modeling techniques to these newly compiled vertical transects, we develop a consistent approach to identifying the onset of faulting within the RGR.

Rift initiation has also historically been identified by the onset of voluminous volcanism or eruption of specific magmatic compositions, namely, mafic or bimodal volcanism (e.g., Bailey, 1974; Cosca et al., 2014; Johnson & Thompson, 1991; Kellogg, 1999; Ricketts et al., 2015; Tweto, 1979), although recent studies from the East African rift imply that volcanism cannot necessarily be used as a proxy for rift activity (e.g., Corti et al., 2019). Therefore, we assemble published data on Cenozoic volcanic rocks in Colorado and New Mexico to summarize and evaluate spatial, temporal, and compositional patterns in magmatism and compare the spatiotemporal patterns of rift-related volcanism to the fault initiation and exhumation patterns determined from the thermochronometry data.

Tectonics

10.1029/2019TC005635

Table 1
Summary of Information From Each Rio Grande Rift Basin

Faulting	Sedimentation	Magmatism	Low-temperature thermochronometry	Rifting interpretations
Southern Rio Grande rift				
Palomas Basin				
Caballo Fault (W)[3]	Primarily from the Black Range[1]	Mogollon-Datil VF (late Eocene to early Miocene)	Black Range: AFT 20–40 Ma[1]; ZFT ~68 Ma[1]; AHe 45–52 Ma[2] Caballo Mountains: AFT 5–18 Ma[1]	• Rift related exhumation primarily occurred on the east side of the basin and AFT suggest that the PAZ was 3–3.5 km deep in the late Eocene.[1]
Jornada Basin				
Jornada Draw Fault (E)[3]	Primarily from the San Andreas Mountains[1]	Jornada del Muerto VF (Quaternary) Potrillo VF (Quaternary)	Sparse data in the central and southern part of the basin and Las Uvas Mountains: 6–18 Ma[1]	• Rapid erosion and fault block tilting occurred in the middle Miocene.[1]
Tularosa Basin				
San Andreas Fault (60°? E)[1,3] Alamogordo Fault (W)[3]	2–3 km thick[30]	Carrizozo VF (Quaternary)	San Andreas Mountains: ZFT 49 Ma[1]; AFT 8–22 Ma[1]; AHe 9–16 Ma[2] Organ Mountains: AFT 10–29 Ma[1]; AHe 10–16 Ma[2] Sacramento Mountains: AFT 40–67 Ma[1] Sierra Blanca intrusion: AFT 23–33 Ma; AHe 15–23 Ma[2]	• Onset of rifting indicated by the younger AFT in Sierra Blanca and suggests rapid denudation rates of 200-400 m/Myr.[1] • Combined the AFT and AHe data imply that rapid cooling and rift extension occurred between 25 and 10 Ma.[2]
Southern Albuquerque Basin				
La Jencia Fault (80–85°E)[3,4] Ladron Fault (E)[5] Jeter fault (15–30°E)[5] Coyote Springs Fault (E)[3] Santa Fe Fault (E)[3] Socorro Canyon (E)[3] Loma Pelada Fault (E)[3] West Joyita Fault (W)[3] Los Piños fault (W)[3,6] Manzano Fault (W)[3,6]	Basin fill is mostly middle Miocene age and includes the Popotosa fm. and Santa Fe fm. (interbedded with 14.5 Ma volcanic rocks[32]). Rift fill thicknesses are ~8 km[8,31]	Socorro Magma Body (subsurface)[5,40,41]	Magdalena Mountains: AFT 46–4 Ma[6] Lemitar Mountains: AFT 13–6 Ma[6] Sierra Ladrones: AFT 32–9 Ma[6]; AHe ~9–12 Ma[5] Joyita Hills: AFT 8–26 Ma[6]; AHe ~18 Ma[2] Los Piños Mountains: AFT 37–65 Ma[6] Manzano Mountains: AFT 20–47 Ma[6]; AHe 25–41 Ma[2]	• Two phases of exhumation (1) late Laramide, (2) post-18 Ma.[7] • Two phases of rift exhumation (1) late Oligocene to early Miocene, (2) middle Miocene to Present.[8] • Continuous exhumation 25–2 Ma with high rates 20–10 Ma and slower rates 10–5 Ma.[5]
Central Rio Grande rift				
Northern Albuquerque Basin				
Knife Edge Fault (W)[3,5,7,9] Rincon Fault (W)[5] San Francisco Fault (NW)[3,7,9] La Bajada Fault (W)[3,7,9] Sand Hill Fault zone (E)[3]	Santa Fe Fm. at the base of the Sandias (interbedded with 16.1 Ma basalt flows); ~4,200 m thick[9,33,34]	Lucero VF, Albuquerque-Cat Hills VF, San Felipe VF, Cienega VF (late-Miocene to Quaternary)	Sandia Mountains: AFT 15–30 Ma[7] and 16–22 Ma[9]; AHe 12–18 Ma[9] Ortiz Mountains: AFT 25–32 Ma[9]; AHe 17–18 Ma[9]	• Rapid cooling in two phases (1) 22–17 Ma and (2) 14–13 Ma.[9] • The 3.1 km of material was exhumed, and 2.4 km of rock uplift has occurred in the Sandia Mountains since the middle Miocene.[9]
Española Basin				
Pajarito Fault (E) [3,10,43] Embudo Fault (left-lateral)[3,10, 43]	Santa Fe fm. ~3 km thick on the west side of the basin[33, 42, 43] and 2 km thick on the east side[10, 42, 43]	Mount Taylor VF, Jemez VF, Taos Plateau VF, Ocate	Santa Fe Mountains: AFT 55–75 Ma[7]; AHe 44–115 Ma[2]	

10.1029/2019TC005635

Table 1
(continued)

Faulting	Sedimentation	Magmatism	Low-temperature thermochronometry	Rifting interpretations
Picuris-Pecos Fault (W) [3,10] Tijeras Fault (left-lateral) [3,9,10] Nambe Fault (W)[3]		VF (late-Miocene to Quaternary)	Nacimiento Mountains: AFT (south) 46–33 Ma[6]; AFT (north) 81–46 Ma[6]	• Cooling in the Santa Fe Mountains occurred during the Laramide Orogeny.[11]
Northern Rio Grande Rift				
San Luis Basin				
Sangre de Cristo Fault (60–70°W)[3,6,7,10,12,13]	Santa Fe Fm. was deposited from 26–2 Ma[35,36] Sedimentation peaks in middle to late Miocene [15,18,19,36] Thicknesses: ~3 km over the Alamosa horst in the center of the basin[35,37] and up to 9 km at the basins edges [12,15,35,37]	Taos Plateau VF (late-Miocene to Quaternary), San Juan VF (late-Eocene to early Miocene)	Sangre de Cristo Mountains: AFT (south) 18–34 Ma[7]; AHe (central) 9–33 Ma[2]; AFT (north) 15–23 Ma[12,13]; AHe (north) ~11 Ma[2]	• Multiphase cooling in the southern Sangre de Cristo Mountains: (1) Laramide-driven cooling and exhumation from the late Cretaceous to early cenozoic[6,11] (2) rift-initiated cooling from the Oligocene to Miocene[6,11,12,13,14] (3) continued rifting from late Miocene to present.[11,12,13,15.16,17,18,19] • Rapid cooling occurs from 28–0 Ma[2] in the central Sangre de Cristo Mountains • Late Laramide cooling pulse followed by a rifting pulse from the late Oligocene to early Miocene[11], in the northern Sangre de Cristo Mountains • Rifting was not fully established until the Miocene.[13,14]
Upper Arkansas River Basin				
Sawatch Range Fault (70°E)[20,27]	Dry Union Fm.: late Miocene[38]; 900–1,800 m thick[18,26,39,38]	San Juan VF, 39 Mile VF (late-Eocene to early Miocene)	Sawatch Range: AFT 9–37 Ma[6,21,22,23]; AHe 2–33 Ma[2,20] Arkansas Hills: AHe 54–65 Ma[24] Mosquito Range (south): AHe 59–260 Ma[24]	• Fault initiation ~28–29 Ma[15,21] • Continuous rapid cooling from 28 to 5 Ma[2] • Pulsed exhumation (1) 22–16 Ma and (2) 8–0 Ma[20,25,26]
Blue River Basin				
Blue River Fault (50-75°E)[27,28]	Deposition began ~27 Ma and continued until at least the early Miocene[29]	North Park VF (late-Eocene to early Miocene), Flat Top VF (Miocene), Yampa VF (late-Miocene)	Williams Fork Mountains: AFT 21–37 Ma[29] Gore Range: AFT (east) 5–20 Ma[29]; AHe (east) 5–20 Ma[28]; AFT (west) 17–37 Ma[29]; AHe (west) 27–51 Ma[28]	• Fault initiation in the Oligocene followed by cooling and unroofing until at least 7 Ma with 2.3 km of displacement on the Blue River Fault and 3–5.4 km of exhumation.[28]

Note. VF = volcanic field; AFT = apatite fission track; ZFT = zircon fission track; AHe = apatite (U-Th)/He; PAZ = partial annealing zone.
[1]Kelley and Chapin (1997). [2]Ricketts et al. (2016). [3]Machette et al., 1998. [4]Machette, 1988. [5]Ricketts et al., 2015. [6]Kelley et al., 1992. [7]Kelley & Duncan, 1986. [8]Lewis & Baldridge, 1994. [9]House et al., 2003. [10]Grauch et al., 2017. [11]Kelley, 1990. [12]Lindsey et al., 1983. [13]Lindsey et al., 1986. [14]Kelley & Chapin, 1995. [15]Tweto, 1979. [16]Chapin & Seager, 1975. [17]Morgan et al., 1986. [18]Taylor, 1975. [19]Epis et al., 1976. [20]Abbey & Niemi, 2018. [21]Shannon, 1988. [22]Bryant & Naeser, 1980. [23]Cunningham et al., 1977. [24]Abbey et al., 2017. [25]Hubbard et al., 2001. [26]Knepper, 1974. [27]Morgan, 2017. [28]Landman & Flowers, 2013. [29]Naeser et al., 2002. [30]Peterson and Roy, 2005. [31]Lozinsky, 1988. [32]McIntosh & Quade, 1995. [33]Chapin & Cather, 1994. [34]May & Russell, 1994. [35]Brister & Gries, 1994. [36]Smith, 2004. [37]Kluth & Schaftenaar, 1994. [38]van Alstine, 1969. [39]Scott, 1975. [40]Sanford et al., 1977. [41]Balch et al., 1997. [42]Koning et al., 2016. [43]Biehler et al., 1991.

2.2. Physiography of the RGR

Physiographic characteristics (e.g., narrow or wide grabens, asymmetric or symmetric faulting, voluminous volcanism vs. lack of magmatism, and/or changes in graben trend/strike) within continental rifts are partially attributed to differences in extensional accommodation mechanisms, which in rift systems, can be either faulting, magmatism, or a combination of the two (e.g., Buck, 2004; Ebinger et al., 2013; Lavecchia et al., 2017; Molnar et al., 2017; Muirhead et al., 2016; Reyners et al., 2007). The RGR is a >1,000-km-long continental rift that extends from potentially as far south as the Big Bend area on the Texas-Mexico Border (e.g., Muehlberger et al., 1978; Nakai et al., 2017; van Wijk et al., 2018), through New Mexico to central Colorado (Figure 2; Kelley et al., 1992; Knepper, 1974; Limbach, 1975), and possibly as far north as southern Wyoming, USA (e.g., Cosca et al., 2014; Kellogg, 1999; Leonard et al., 2002; Naeser et al., 2002; Nakai et al., 2017). The majority of the basins formed from RGR extension are asymmetric half grabens (Kellogg, 1999) with significant exhumation occurring along north-south striking basin-bounding normal fault systems connected by various ACZs (Figures 2 and 6; Lewis & Baldridge, 1994; Kellogg, 1999; Naeser et al., 2002; Ricketts et al., 2016). The surface expression of the RGR varies from north to south, displaying distinct physiographic differences (Ingersoll, 2001). The southern RGR is composed of several wide asymmetric grabens at a given latitude, each basin is bounded by a single north-south striking normal fault, and this region has minor Quaternary volcanism. The central RGR is bound by northeast-southwest striking left-lateral strike-slip faults. There are also numerous north-south striking intrabasin normal faults with little vertical offset and voluminous Miocene to Quaternary volcanism. The northern RGR is characterized by narrow asymmetric grabens bounded by a single north-south striking normal fault at a given latitude and is nearly entirely devoid of rift-related volcanism. Such remarkable differences in the surface expression of rifting lead us to question whether or not the physiography of the RGR might provide insight into the development and evolution of the RGR and emphasize the need to explore patterns of both faulting and magmatism holistically along the entire rift system.

3. Summary of Thermochronometry, Magmatism, and Extension in the RGR

Because we are interested in determining information about both the timing of rift initiation and about rift extension accommodation mechanisms, we summarize faulting and magmatism information from each RGR basin below. We focus on low-temperature thermochronometry data sets, which provide details on fault growth, and spatiotemporal relationships in magmatism, which offer insight into extension accommodation via dike injection rather than normal faulting. We acknowledge that basin sedimentation is another useful proxy for information on basin development and rift timing; however, because synrift sedimentation is not well dated throughout the entire RGR and is not necessarily helpful in distinguishing between accommodation mechanisms, we do not go into those details in the text and instead include published information about basin sedimentation timing, source, and thicknesses in Table 1.

3.1. Southern RGR

The southern RGR exhibits the greatest amounts of horizontal extension in any section of the rift, with 50% extension accommodated by several grabens at a given latitude (i.e., the Palomas, Jornada, and Tularosa basins; Chapin & Cather, 1994; Figures 2 and 3). The individual basins range in size from ~20 to 50 km wide and ~80 to 150 km long. The faults bounding these basins are north-south striking high angle (>60° dips) normal faults.

Published low-temperature thermochronometry data from the basin-bounding ranges include minimal AFT and AHe data showing early Cenozoic ages in the mountain ranges not bound by active faults and Miocene cooling ages in the mountain ranges uplifted by active extensional faults (Table 1 and Figure 3; Kelley & Chapin, 1997; Ricketts et al., 2016).

Late Cenozoic volcanism within the southern RGR is sparse, represented by several minor Quaternary basalt flows (the Jornada del Muerto, Carrizozo, and Potrillo volcanic fields; Figure 6; McMillan et al., 2000; NM Bureau of Geology and Mineral Resources, 2003). To the west of the three southernmost basins are the mid-Cenozoic Mogollon-Datil ignimbrites, which are attributed to slab retreat and slowing plate convergence rates at the end of the Laramide Orogeny and are assumed to predate the onset of RGR extension (Figure 6; McMillan et al., 2000; Chapin et al., 2004).

The northernmost basin in the southern RGR is the southern Albuquerque Basin, which we define as the area from south of Socorro, NM, to Albuquerque, NM (Figures 2 and 3). It is the widest of any of the individual rift basins in the RGR spanning ~80 km from east to west and has undergone ~28% extension (Chapin & Cather, 1994; Russell & Snelson, 1994). This basin contains numerous high angle (>70–80°) faults along several small mountain ranges (Figure 3 and Table 1; Machette, 1988; Ricketts et al., 2015).

Low-temperature thermochronometry data from these mountains show that the western side of the basin is dominated by Oligocene to Miocene cooling ages, whereas the eastern side of the southern Albuquerque Basin preserves Paleocene to Oligocene cooling ages (Table 1 and Figure 3; Kelley et al., 1992; Ricketts et al., 2015; Ricketts et al., 2016). At the base of the Magdalena Mountains, we collected a sample for ZHe analysis and obtained a cooling age of 14.4 ± 0.6 Ma (Tables 2, 3, and S1 in the supporting information and Figure 3).

Although there are several low-volume extrusive deposits in the southern Albuquerque Basin, there is no significant rift-related volcanism. However, the southern Albuquerque Basin is known to be underlain by the Socorro magma body, at a depth of ~19 km and comprising an area of ~3,400 km^2. This magma body is the cause for much of the present-day seismicity in central New Mexico (Balch et al., 1997; Nakai et al., 2017; Sanford et al., 1977).

3.2. Central RGR

The central RGR encompasses a transition from rift-extension dominated by large basin-bounding normal faults and minor magmatism to a section controlled by strike-slip faulting, minor intrabasin faults, and voluminous volcanism (Figures 4 and 7; Koning et al., 2016; Grauch et al., 2017). The central RGR includes the northern Albuquerque Basin (Albuquerque, NM, to Santa Fe, NM) and the Española Basin (Kelley, 1979; Figure 4). The style of faulting in the central RGR is significantly different from that in the southern RGR. The central RGR is bound by two northeast-southwest striking left-lateral strike-slip faults: the Embudo fault, which has accommodated left-lateral slip since ~12–11 Ma (Grauch et al., 2017; Kelson et al., 2004; Koning et al., 2016), although it also has a significant amount of normal motion to the south (Brown & Golombek, 1986; Liu et al., 2019), and the Tijeras fault (Figure 4). In addition to these large strike-slip faults, the Sandia Mountains have been uplifted on the east side of the northern Albuquerque Basin by several normal faults, most prominently, the high-angle Rincon fault and tilted Knife Edge fault (Kelley & Duncan, 1986, Machette et al., 1998; House et al., 2003; Ricketts et al., 2015; Table 1 and Figure 4). Both the northern Albuquerque and Española basins are characterized by a distributed set of north-south striking intrabasin normal faults (~10–20 km long), which accommodate minimal vertical offset (Figure 4; Machette et al., 1998; Grauch et al., 2017; Liu et al., 2019). Horizontal extension in the northern Albuquerque Basin is 17% (Chapin & Cather, 1994), and no known extension estimates are available for the Española Basin.

Low-temperature thermochronometry data from the central RGR reveal Miocene cooling on the east side of the northern Albuquerque Basin (Table 1 and Figure 4; Kelley & Duncan, 1986; House et al., 2003), but cooling ages range from the late Cretaceous to the Eocene surrounding the Española Basin (Table 1 and Figure 4; Kelley & Duncan, 1986; Kelley et al., 1992; Ricketts et al., 2016). We collected a sample at the base of the Santa Fe Mountains for AHe analysis, which yielded a cooling age of 58.7 ± 3.6 Ma (Tables 2, 3, and S1 and Figure 4).

Late Cenozoic (<10 Ma) volcanism in the central RGR is voluminous, with compositions ranging from felsic to mafic (Figures 6 and 7). The spatial extent of this young volcanism is not confined to the rift boundaries but extends along a northeast-southwest trend from Arizona to Kansas, following the Jemez Lineament (Figure 6; e.g., NM Bureau of Geology and Mineral Resources, 2003; Chapin et al., 2004; Grauch et al., 2017).

3.3. Northern RGR

The northern RGR is relatively narrow in comparison to the basins of the southern and central RGR and is composed of three en echelon grabens (from south to north, the San Luis, upper Arkansas River [UAR], and Blue River grabens), each bounded by a single normal fault, forming an asymmetric half graben (Figure 5). The three basins range from 5 to 75 km wide and 60 to 200 km in length, with high angle (>60°) north-south striking normal faults producing high-relief mountains along the basin flanks (Figures 2 and 5; Miller, 1999; U.S. Geological Survey, 2006; Landman & Flowers, 2013; Morgan, 2017; Abbey & Niemi, 2018). The basin bounding faults in the northern RGR are hypothesized to be reactivated Laramide structures (Ingersoll, 2001; Liu et al., 2019; Tweto, 1979). Extension estimates in the northern RGR are 8–12% in the San Luis

Basin (Chapin & Cather, 1994; Kluth & Schaftenaar, 1994) with no estimates published for the UAR or Blue River basins. The basins in the northern RGR have little internal deformation (Kluth & Schaftenaar, 1994) although there is a central horst (Alamosa Horst) in the middle of the San Luis Basin that causes the deepest parts of the basin to be on the flanks (Brister & Gries, 1994; Kluth & Schaftenaar, 1994).

Low-temperature thermochronometry cooling ages in the footwalls of the normal faults that define the northern RGR grabens reveal that fault exhumation initiated in the Oligocene, continued to at least the late Miocene and that in some places exhumation continued into the Quaternary (UAR Basin; Table 1 and Figure 5; Cunningham et al., 1977; Bryant & Naeser, 1980; Lindsey et al., 1983; Lindsey et al., 1986; Kelley & Duncan, 1986; Shannon, 1988; Kelley et al., 1992; Naeser et al., 2002; Landman & Flowers, 2013; Ricketts et al., 2016; Abbey & Niemi, 2018). In contrast to the relatively young cooling ages on the faulted sides of the northern RGR half grabens, cooling ages on the passive sides of these grabens are substantially older, ranging from Cretaceous to Eocene (Naeser et al., 2002; Landman & Flowers, 2013; Abbey et al., 2017; Figure 5).

New AHe ages from the base of the southern and northern Sangre de Cristo Mountains are 8.8 $\pm$ 0.5 and 7.4 $\pm$ 0.5 Ma, respectively, and a new ZHe age from the base of the central Sangre de Cristo Mountains is 19.4 $\pm$ 0.4 Ma (Tables 2, 3, and S1 and Figure 5).

Rift-related volcanism in the northern RGR basins is essentially nonexistent, with the exception of the Miocene-aged Taos Plateau volcanic field blanketing the basin fill in the southernmost part of the San Luis Basin (Figure 6). On the west and east margins of the rift, respectively, are the expansive Eocene-Oligocene San Juan and Thirty-nine Mile volcanic fields, which, as with the Mogollon-Datil volcanic field in southern New Mexico, are interpreted to be related to flat-slab-subduction and roll-back at the end of the Laramide orogeny (Chapin et al., 2004). Sparse volcanic deposits with rift-related chemical signatures and ages of <6 Ma exist about 50 km west of the northernmost rift basin (Blue River Basin) in the northern RGR (Figure 6; Leat et al., 1989, 1990; Cosca et al., 2014). Recent seismicity, along with these volcanic rocks and extensional features (faults) similar in age to rifting (Tweto, 1979), suggests the possibility that the rift extends as far north as Wyoming (Nakai et al., 2017). However, no clearly defined range-bounding normal faults north of those studied here have been identified as targets for low-temperature thermochronometry sampling.

4. Results and Interpretations From Inverse Thermal History Modeling of Low-Temperature Thermochronometry Data

Inverse thermal history modeling provides a way to explore many possible cooling histories for a given sample or group of samples to resolve exhumation histories from low-temperature thermochronometric data. The power of this approach is magnified when samples with varying closure temperatures and/or with known vertical spatial relationships can be jointly inverted to find a cooling history that satisfies the data obtained from all of the samples. The more vertical space covered along the exhumed fault block then the more information can be gleaned about the initiation of fault motion as well as the minimum temperatures to which the rocks were exposed at depth.

We use the program QTQt (QTQt64R5.6.2a; Gallagher, 2012) for inverse thermal history modeling of 14 compiled vertical transects composed of thermochronometry data from 130 samples along the RGR (Figures 3–5 and Table 3). QTQt has the ability to incorporate multiple samples with a known spatial relationship (i.e., vertical transects) and can invert for thermal histories from different thermochronometers simultaneously within the same model. A multisample modeling approach allows for identification of thermal histories that satisfy the observed data, geologic assumptions, and model constraints, which helps to avoid unjustified structure of a thermal history that can occur when overfitting data from an individual sample (Gallagher et al., 2005). The outputs from these inverse thermal history models are the "most-likely" time-temperature paths that a sample or group of samples may have undergone (Figures 3–5), which helps to resolve questions related to timing, magnitudes, and rates of exhumation along the faults adjacent to which the samples were collected.

We assume sample location relationships did not change as the rocks were exhumed to the surface and that each sample in the transect has experienced the same exhumation history. However, exhumation along a

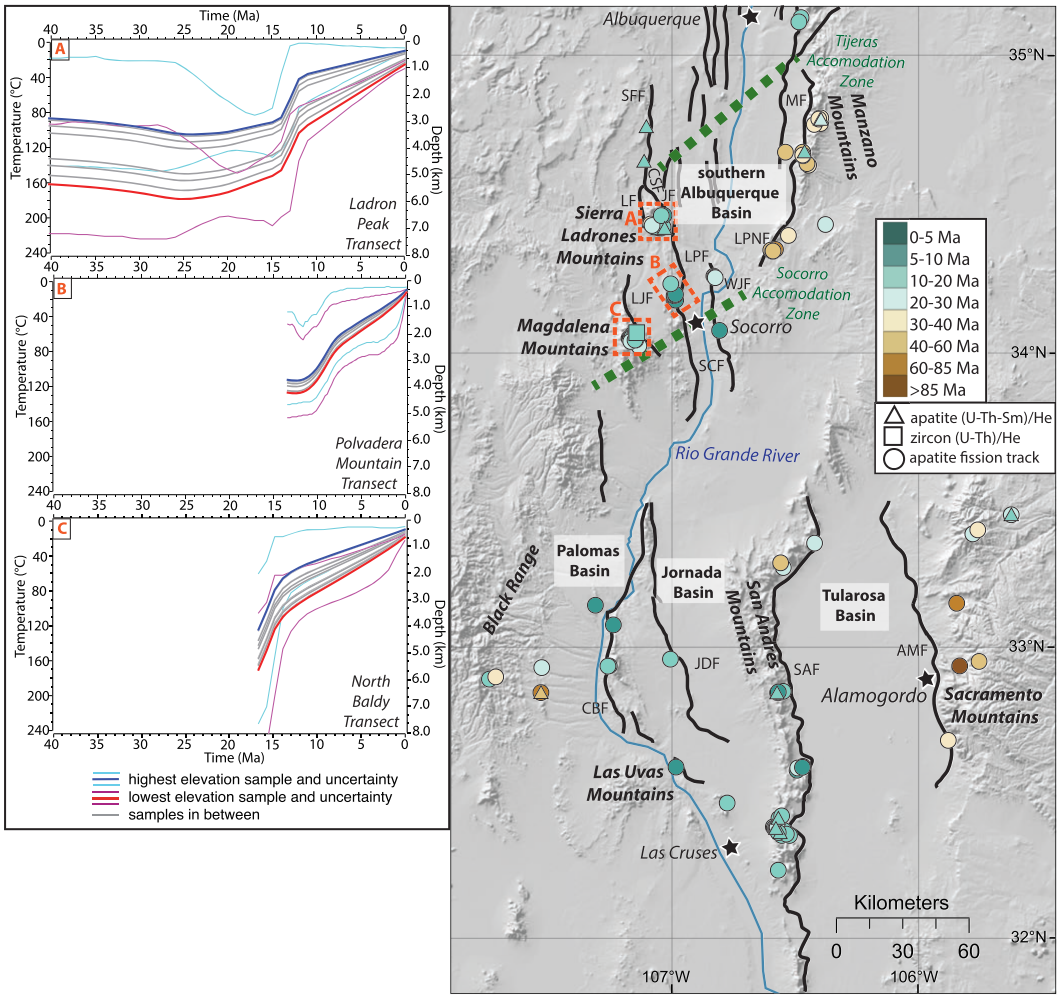

Figure 3. Southern Rio Grande rift (RGR). Low-temperature thermochronometry (previously published: Tables 1 and 3 and this study) colored by cooling age. Inverse thermal history modeling was performed for three vertical transects from the southern Albuquerque basin, where samples were determined suitable for inverse thermal modeling as described in the text (dashed orange boxes and letters: (a) Ladron Peak transect; (b) Polvadera Mountain transect; (c) North Baldy transect; Table 3). Model fits between observed and predicted data shown in Figure S2. Accommodation zones indicated by dashed green lines and major faults named with the following abbreviations: LJF = La Jencia fault; LPF = Loma Pelada fault; CBF = Cabaillo fault; SAF = San Andreas Fault; AMF = Alamagodo fault; SCF = Socorro Canyon fault; WJF = West Joyita fault; MF = Manzano fault; Loma Paleda fault, LF = Ladron fault; JF = Jeter fault; CSF = Coyote Springs fault; SFF = Santa Fe Fault; LPNF = Los Pinos fault.

normal fault implies the footwall samples have experienced some amount of tilting that is related to the dip of the fault (Johnstone & Colgan, 2018; Shirvell et al., 2009; Stockli et al., 2000), which means the paleovertical distance between the samples is different from the present-day vertical distance. To account for this difference in paleovertical versus modern vertical distance between samples, we project the samples from a single transect onto the fault plane on which they were exhumed (Abbey & Niemi, 2018). This projection allows us to determine the fault-parallel distance (i.e., the paleovertical distance between the samples) at the time the samples underwent exhumation. These fault-parallel distance relationships are input as pseudo-elevations in our inverse thermal history models (Table 3).

4.1. Fault Initiation and Exhumation in the RGR

4.1.1. Southern RGR

The three southernmost RGR basins (Palomas, Jornada, and Tularosa) do not have any thermochronometry samples that fit our criteria for a vertical transect, so we did not perform any inverse thermal history modeling on data from those basins. We note, however, that the cooling ages from the thermochronometric data on the active basin-bounding faults are generally between ~20 and 5 Ma (Figure 3; Kelley & Chapin, 1997;

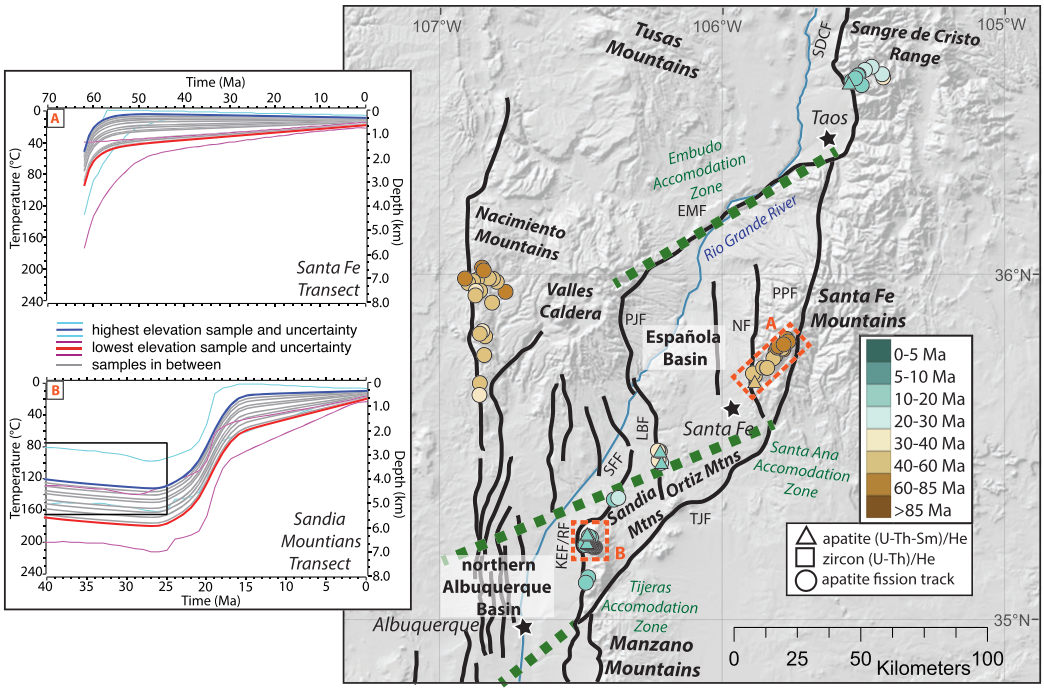

Figure 4. Central Rio Grande rift (RGR). Low-temperature thermochronometry (previously published: Tables 1 and 3 and this study) colored by cooling age. Inverse thermal history modeling was performed for two vertical transects from the Española basin, where samples were determined suitable for inverse thermal modeling as described in the text (dashed orange boxes and letters: (a) Santa Fe transect and (b) Sandia Mountains transect; Table 3). Model fits between observed and predicted data shown in Figure S2. Accommodation zones indicated by dashed green lines and major faults named with the following abbreviations: PJF = Pajarito fault; SDCF = Sangre de Cristo fault; PPF = Picuris-Pecos fault; LBF = La Bajada fault; SFF = San Francisco fault; KEF = Knife edge fault; RF = Rincon fault; TJF = Tijeras fault; NF = Nambe fault.

Ricketts et al., 2016). Although we cannot determine fault initiation timing and rates or magnitudes of exhumation, we can use these data to infer that fault exhumation occurred during the Miocene in the southernmost RGR basins.

4.1.1.1. Southern Albuquerque Basin

Three vertical transects were identified and used for inverse thermal history modeling in the southern Albuquerque Basin (Table 3). The North Baldy transect from the Magdalena Mountains includes AFT data from Kelley et al. (1992) and ZHe data from this study (Table 3) and constrains exhumation on the La Jencia fault, with the earliest onset of faulting at ca. 25 Ma (Figure 3). Exhumation proceedes from ~25 to 19 Ma at a rate of ~0.3 mm/yr and increases to ~0.5 mm/yr from ~19 to 16 Ma. From 16 Ma to present, we cannot resolve a specific pulse of cooling; however, fault exhumation continued at an average rate of 0.2 mm/yr (Figure 3). The total magnitude of exhumation recorded from the North Baldy transect is ~7 km (Figure 3).

The Polvadera Mountain transect, from the Lemitar Mountains, is composed of AFT data from Kelley et al. (1992) and records exhumation on the Socorro Canyon fault (Table 3 and Figure 3). Fault initiation appears to occur at ~12 Ma, at an exhumation rate of ~0.4 mm/yr until ~8 Ma, at which point the exhumation rate decreases to an average of 0.3 mm/yr from 8 to 0 Ma (Figure 3). Total exhumation on this fault segment was >4 km (Figure 3).

To the north, along the Loma Pelada fault, the Ladron Peak transect includes AFT data from Kelley et al. (1992) and AHe data from Ricketts et al. (2015) (Table 3). Fault initiation occurs at ~14 Ma, exhuming the footwall at a rate of ~0.7 mm/yr from 14 to 11 Ma followed by slower exhumation at an average rate of 0.2–0.3 mm/yr from 11 Ma to present (Figure 3). The magnitude of exhumation recorded by the Ladrom Peak transect is ~5 km (Figure 3).

4.1.2. Central RGR

4.1.2.1. Northern Albuquerque Basin

We performed inverse thermal history modeling on one group of AFT and AHe samples (House et al., 2003; Kelley & Duncan, 1986) exhumed on the Knife Edge fault at the base of the Sandia Mountains (Table 3 and

Figures 4 and 6). This model incorporates a constraint box to account for burial estimates made by House et al. (2003), who suggest that ~2.4 km of section was overlying the Sandia Mountains at the end of the Cretaceous and that another 1–2.5 km was added to that cover during the end of the Laramide Orogeny. Motion along the Knife Edge fault appears to initiate at ~24 Ma, with exhumation proceeding until ~16 Ma at a rate of ~0.4 mm/yr, bringing rock from ~5 km depth to within <1 km of the surface. From ~16 Ma to present, there is <1 km of exhumation recorded in the Sandia Mountains (Figure 4).

4.1.2.2. Española Basin

Thermochronometric ages in and around the Española Basin range from ~80 to ~30 Ma (Figure 4; Kelley & Duncan, 1986; Kelley et al., 1992; House et al., 2003). Thermal history modeling of the Santa Fe transect with AFT data from Kelley and Duncan (1986) and AHe data from this study shows that all of the samples were close to reasonable surface temperatures by ca. 50 Ma (Table 3 and Figure 4), which suggests that the Nambe Fault at the range front of the Santa Fe Mountains does not accommodate a large enough amount of rift-related vertical fault displacement to detect with low-temperature thermochronometry methods. Thus, the timing of exhumation adjacent to and in the vicinity of the Española Basin seems to be entirely associated with the Laramide Orogeny in agreement with Baldridge et al. (1994). This places a limit on rift related exhumation of less than ~1.5 km in the western Santa Fe Mountains.

4.1.3. Northern RGR

4.1.3.1. San Luis Basin

In the San Luis Basin, we identified three groups of samples that fit our criteria for a vertical transect (Figure 5 and Table 3). In the southern San Luis Basin, the Wheeler Peak transect includes AFT data from Kelley and Duncan (1986) and AHe data from this study and shows fault exhumation at a rate of ~0.4 mm/yr from 25 to 20 Ma. Post-20 Ma, the thermal history modeling does not recover any discrete pulses of cooling, and exhumation occurs at an average rate of 0.2 mm/yr. Overall, >6 km of exhumation is recorded by the Wheeler Peak transect (Figure 5).

In the north-central part of the San Luis Basin, the Sand Dunes transect incorporates AHe, AFT, and ZHe data (Kelley & Duncan, 1986; Ricketts et al., 2016; and this study; Figure 5 and Table 3) and reveals fault initiation at ~14 Ma at an exhumation rate of ~1.0 mm/yr from 14 to 11 Ma. From 8 Ma to present, footwall rocks exhumed from ~4-km depth at a rate of 0.5 mm/yr. This transect records >7 km of exhumation (Figure 5).

The northernmost vertical transect in the San Luis Basin, the Mount Owens transect, includes AFT and AHe data (Lindsey et al., 1986; and this study; Table 3) as well as a constraint to represent conodont analyses from Lindsey et al. (1986) that indicates burial to temperatures of 200–300 °C (Figure 5). Thermal history modeling shows that from ~25 to 20 Ma, fault exhumation occurred at a rate of 0.4 mm/yr. After 20 Ma, the footwall continued to exhume at an average rate of ~0.15–0.2 mm/yr until the present day, with no discrete pulses or changes in exhumation recovered over this time period. Total exhumation recorded by the Mount Owens transects is >5 km (Figure 5).

4.1.3.2. UAR Basin

The UAR Basin has the highest density of published low-temperature thermochronometry data, and we identified four transects useful for assessing rift-related exhumation (Table 3). In the south, the Mount Shavano transect includes AHe and AFT data (Shannon, 1988; and Abbey & Niemi, 2018; Table 3) and reveals fault initiation at ~16 Ma, exhuming at a rate of ~0.5 mm/yr until ~12 Ma. After ~12 Ma, exhumation rates slow, and discrete cooling pulses are not captured in the model, although exhumation continues at an average rate of <0.2 mm/yr. The Mount Shavano transect records ~4 km of exhumation (Figure 5).

In the south-central part of the Sawatch Range fault system, the Mount Princeton transect, which includes ZHe, AFT, and AHe data (Kelley et al., 1992; Ricketts et al., 2016; and Abbey & Niemi, 2018; Figure 5 and Table 3), records fault initiation at ~24 Ma. Rapid exhumation occurred at a rate of ~0.6 mm/yr until ~19 Ma. A second pulse of exhumation began at ~5 Ma, exhuming rock from to the surface at a rate of ~0.7 mm/yr. This transect records >7 km of exhumation (Figure 5).

In the northern part of the Sawatch Range, the Mount Belford transect, composed of AHe and ZHe data (Abbey & Niemi, 2018; Table 3), records onset of cooling at ~20 Ma, although no distinct cooling pulses are discernable in the thermal history post-20 Ma. Samples were exhumed a total of ~4 km at an average rate of 0.2 mm/yr from 20 Ma to present (Figure 5).

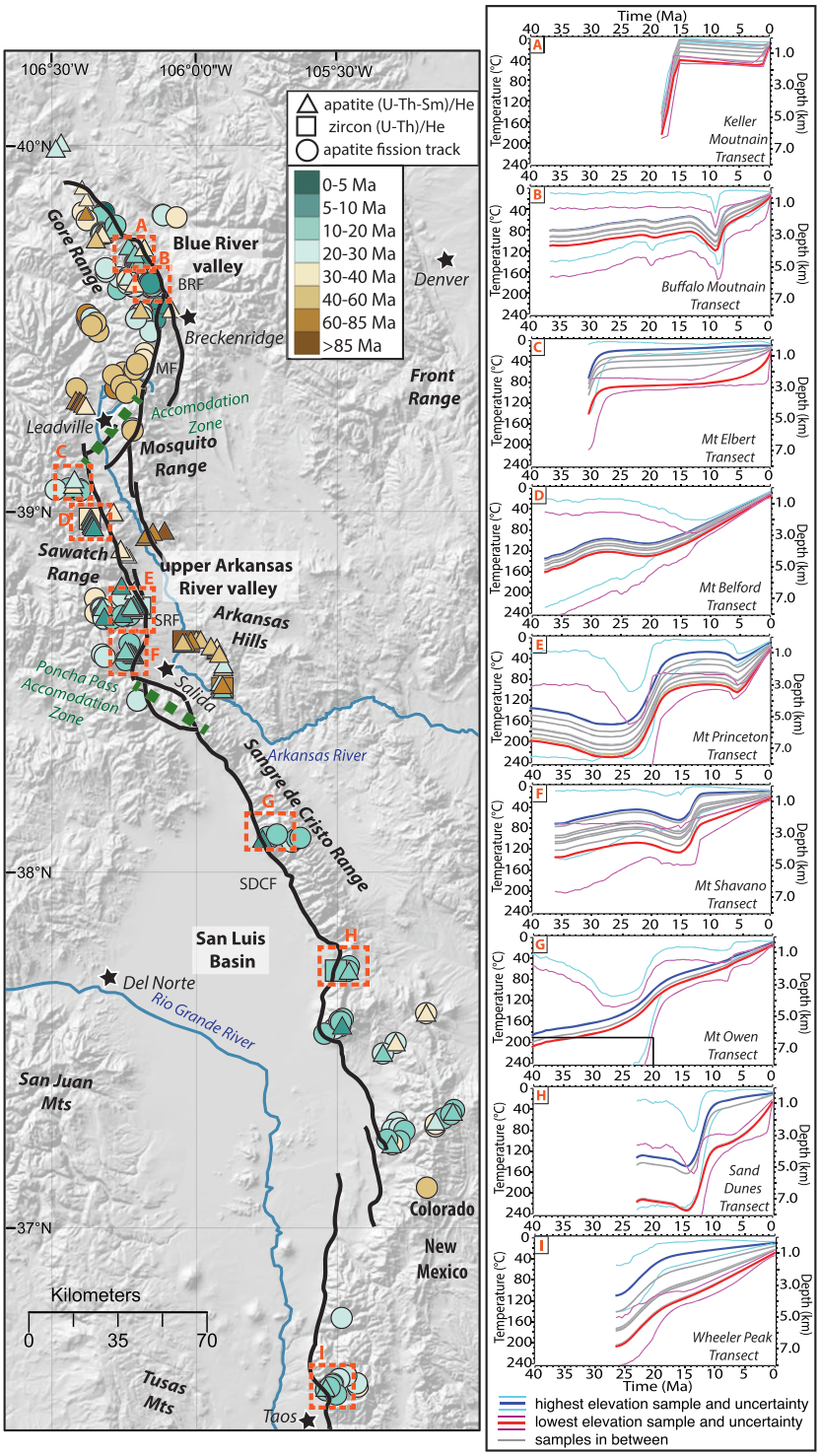

Figure 5. Northern Rio Grande rift (RGR). Low-temperature thermochronometry (previously published: Tables 1 and 3 and this study) colored by cooling age. Inverse thermal history modeling was performed for three vertical transects from the San Luis basin, four vertical transects from the upper Arkansas River basin, and two vertical transects from the Blue River basin (dashed orange boxes and letters: (a) Keller Mountain transect; (b) Buffalo Mountain transect; (c) Mount Elbert transect; (d) Mount Belford transect; (e) Mount Princeton transect; (f) Mount Shavano transect; (g) Mount Owen transect; (h) Sand Dunes transect; (i) Wheeler Peak transect; Table 3). Model fits between observed and predicted data shown in Figure S2. Accommodation zones indicated by dashed green lines and major faults named with the following abbreviations: SDCF = Sangre de Cristo fault; SRF = Sawatch Range fault; MF = Mosquito fault; BRF = Blue River fault.

Table 2
Sample Locations and Mean Ages for Apatite (U-Th-Sm)/He and Zircon (U-Th)/He

Sample name	Longitude	Latitude	Elevation (m)	Mineral	Mean age (Ma)
17NSdC	−105.7667	38.1008	2,675	Apatite	7.4 ± 0.5
17SD	−105.5066	37.7334	2,559	Zircon	19.4 ± 0.4
17WEEL	−105.5586	36.5407	2,332	Apatite	11.2 ± 2.4
17SFe	−105.8480	35.6881	2,286	Apatite	58.7 ± 3.6
17NB	−107.1419	34.0764	2,048	Zircon	14.4 ± 0.6

Note. Mean ages and errors are calculated after removal of any outliers (Q-Test; Dean & Dixon, 1951; Table S1).

Table 3
Identified Vertical Transects

Sample name	Ref.	Analysis method	Mean age ± error	Latitude	Longitude	Original elev. (m)	Fault dist. (m)
Keller Mountain transect; Blue River fault (75°E) Blue River Basin, northern RGR							
GRWL1	1	AHe	18.5 ± 0.6	39.6917	−106.2181	3,911	1,234
GRWL2	1	AHe	18.8 ± 1.2	39.6953	−106.2150	3,755	1,013
GRWL3	1	AHe	16.9 ± 0.7	39.6942	−106.2114	3,603	787
GRWL8	1	AHe	11.6 ± 1.0	39.6917	−106.2019	3,230	217
GR-WL-1	2	AFT	15.9 ± 2.2	39.6917	−106.2181	3,911	1,234
GR-WL-2	2	AFT	13.5 ± 2.2	39.6953	−106.2150	3,755	1,013
GR-WL-3	2	AFT	16.8 ± 3.4	39.6942	−106.2114	3,603	787
GR-WL-4	2	AFT	11.9 ± 1.5	39.6936	−106.2075	3,433	536
GR-WL-8	2	AFT	11.7 ± 2.0	39.6917	−106.2019	3,230	217
GR-WL-9	2	AFT	9.2 ± 1.8	39.6908	−106.1978	3,100	0
Buffalo Mountain transect; Blue River fault (75°E); Blue River Basin, northern RGR							
GR-WL-5	2	AFT	8.8 ± 2.6	39.6314	−106.1344	3,066	0
GR-WL-7	2	AFT	6.7 ± 1.5	39.6303	−106.1431	3,152	275
GR-WL-6	2	AFT	10.9 ± 2.4	39.6319	−106.1492	3,364	615
GR-WL-12	2	AFT	11.0 ± 2.8	39.6214	−106.1350	3,621	552
GR-WL-11	2	AFT	19.2 ± 6.7	39.6181	−106.1419	3,871	949
GR-WL-10	2	AFT	19.4 ± 5.1	39.6161	−106.1425	3,889	979
Mount Elbert transect; Sawatch Range fault (70°E); upper Arkansas River Basin, northern RGR							
14MTE-01	3	AHe	11.5 ± 1.1	39.0670	−106.4338	2,973	1,057
14MTE-02	3	AHe	32.2 ± 1.1	39.0803	−106.4353	3,328	1,427
14MTE-05	3	AHe	28.8 ± 0.3	39.0992	−106.4454	4,156	2,036
73 N7	4	AFT	19.9 ± 4.4	39.0731	−106.4508	3,121	1,695
73 N9	4	AFT	16.0 ± 2.4	39.0706	−106.4031	2,819	0
TL-F-6-16	4	AFT	20.0 ± 2.9	39.0656	−106.3997	2,926	5
Mount Belford transect; Sawatch Range fault (70°E); upper Arkansas River Basin, northern RGR							
14MTB-01	3	AHe	7.2 ± 0.5	38.9971	−106.3751	2,957	0
14MTB-01	3	ZHe	33.7 ± 1.6	38.9971	−106.3751	2,957	0
14MTB-02	3	AHe	5.7 ± 0.3	38.9902	−106.3719	3,230	165
14MTB-03	3	AHe	6.8 ± 0.1	38.9812	−106.3731	3,460	422
14MTB-04	3	AHe	5.6 ± 0.5	38.9706	−106.3704	3,692	565
14MTB-04a	3	AHe	8.4 ± 1.2	38.9657	−106.3680	4,001	789
14MTB-05	3	AHe	8.9 ± 0.7	38.9607	−106.3611	4,322	887
Mount Princeton transect; Sawatch Range fault (70°E); upper Arkansas River Basin, northern RGR							
15MTP-01	3	AHe	2.2 ± 0.1	38.7433	−106.1834	2,833	0
15MTP-01	3	ZHe	20.6 ± 0.6	38.7433	−106.1834	2,833	0
15MTP-02	3	AHe	3.0 ± 0.3	38.7420	−106.2017	3,153	836
15MTP-03	3	AHe	7.0 ± 0.8	38.7487	−106.2108	3,450	1,367
15MTP-04	3	AHe	6.3 ± 0.6	38.7369	−106.2144	3,708	1,724
15MTP-05	3	AHe	12.2 ± 1.6	38.7415	−106.2225	3,997	2,210
84MP02	5	AFT	14.1 ± 1.8	38.7420	−106.2007	3,133	793
84MP03	5	AFT	13.2 ± 1.5	38.7422	−106.1928	3,055	485
84MP03	6	AHe	3.1 ± 0.3	38.7422	−106.1928	3,055	485
84MP04	5	AFT	9.5 ± 0.8	38.7428	−106.1865	2,963	210
84MP05	5	AFT	9.6 ± 1.2	38.7485	−106.1873	2,899	172

Table 3
(continued)

Sample name	Ref.	Analysis method	Mean age ± error	Latitude	Longitude	Original elev. (m)	Fault dist. (m)
84MP05	6	AHe	2.7 ± 0.5	38.7485	−106.1873	2,800	172
Mount Shavano transect; Sawatch Range fault (70°E); upper Arkansas River Basin, northern RGR							
15MTS-01	3	AHe	13.9 ± 1.0	38.6031	−106.1984	3,066	0
15MTS-02	3	AHe	10.7 ± 1.1	38.6073	−106.2079	3,292	495
15MTS-03	3	AHe	9.3 ± 1.8	38.6119	−106.2161	3,556	977
15MTS-04	3	AHe	13.9 ± 1.3	38.6139	−106.2261	3,839	1,539
15MTS-05	3	AHe	18.7 ± 1.5	38.6132	−106.2393	4,085	2,181
15MTS-06	3	AHe	10.5 ± 0.4	38.6189	−106.2392	4,341	2,378
84-300_Tag	7	AFT	14.8 ± 2.0	38.6493	−106.2231	3,487	1,110
84-280_Tnfg	7	AFT	19.7 ± 2.7	38.5929	−106.2416	3,158	1,379
Mount Owen transect; northern Sangre de Cristo fault (60°W); San Luis Basin, northern RGR							
G	8	AFT	17.3 ± 5.0	38.1053	−105.7508	2,770	776
H	8	AFT	20.0 ± 4.6	38.1081	−105.7608	2,710	287
17SdC	TS	AHe	7.4 ± 0.5	38.1008	−105.7667	2,675	0
Sand Dunes transect; north/central Sangre de Cristo fault (60°W); San Luis Basin, northern RGR							
88SG01	5	AFT	12.8 ± 2.3	37.7470	−105.4567	3,299	2,784
88SG03	5	AFT	10.4 ± 1.3	37.7307	−105.4612	2,927	2,320
88SG03	6	AHe	11.5 ± 2.2	37.7307	−105.4612	2,927	2,320
88SG05	5	AFT	5.6 ± 1.4	37.7333	−105.5060	2,536	0
17SD	TS	ZHe	19.4 ± 0.4	37.7334	−105.5066	2,559	65
Wheeler Peak transect; southern Sangre de Cristo fault (70°W); San Luis Basin, northern RGR							
81WP7	9	AFT	18.5 ± 3.4	36.5433	−105.5558	2,335	89
NM/H-1	9	AFT	17.6 ± 3.6	36.5533	−105.5287	2,414	997
80 L-6a	9	AFT	11.5 ± 2.2	36.5632	−105.5277	2,457	1,070
81WP6	9	AFT	21.3 ± 3.6	36.5658	−105.5250	2,470	1,164
81WP5	9	AFT	21.8 ± 3.6	36.5830	−105.4972	2,683	2,219
81WP4	9	AFT	22.9 ± 3.6	36.5950	−105.4667	2,805	3,269
17WEEL	TS	AHe	8.8 ± 0.5	36.5407	−105.5586	2,332	0
Santa Fe transect; Nambe fault (near vertical dip W); Española Basin, central RGR							
81SF1	9	AFT	55.1 ± 12.2	35.6983	−105.8988	2,256	N/A
81SF2	9	AFT	57.4 ± 10.6	35.7075	−105.9067	2,296	N/A
81SF3	9	AFT	55.6 ± 11.4	35.7282	−105.8612	2,421	N/A
81SF4	9	AFT	59.0 ± 9.2	35.7267	−105.8452	2,488	N/A
81SF5	9	AFT	61.6 ± 13.4	35.7688	−105.8085	2,985	N/A
81SF6	9	AFT	61.0 ± 8.6	35.7858	−105.8065	3,128	N/A
81SF7	9	AFT	59.4 ± 10.2	35.7620	−105.8162	2,924	N/A
81SF8	9	AFT	68.2 ± 14.2	35.7945	−105.7715	3,732	N/A
81SF9	9	AFT	74.0 ± 12.2	35.7937	−105.7728	3,744	N/A
81SF10	9	AFT	57.6 ± 10.6	35.7973	−105.7973	3,634	N/A
81SF11	9	AFT	62.0 ± 10.6	35.8005	−105.7997	3,610	N/A
81SF12	9	AFT	64.6 ± 10.6	35.8048	−105.7937	3,415	N/A
81SF13	9	AFT	62.9 ± 15.0	35.8320	−105.7580	3,848	N/A
81SF14	9	AFT	69.3 ± 20.0	35.8230	−105.7505	3,543	N/A
81SF15	9	AFT	63.7 ± 16.6	35.8122	−105.7712	3,238	N/A
81SF16	9	AFT	43.8 ± 10.4	35.7272	−105.8440	2,524	N/A
17SFe	TS	AHe	58.7 ± 3.6	35.6881	−105.8480	2,286	N/A
Sandia Mountains transect; Knife Edge fault (70°W); northern Albuquerque Basin, central RGR							
81SAN1	9 & 10	AFT	19.1 ± 2.0	35.2045	−106.4470	3,095	1,639
81SAN1	10	AHe	17.3 ± 1.3	35.2045	−106.4470	3,095	1,639
81SAN2	9 & 10	AFT	21.7 ± 2.3	35.2045	−106.4492	3,006	1,489
81SAN3	9 & 10	AFT	19.3 ± 1.9	35.2045	−106.4515	2,933	1,347
81SAN3	10	AHe	17.1 ± 1.2	35.2045	−106.4515	2,933	1,347
81SAN4	9 & 10	AFT	21.5 ± 1.8	35.2062	−106.4540	2,805	1,150
81SAN4	10	AHe	17.1 ± 0.8	35.2062	−106.4540	2,805	1,150
81SAN5	9 & 10	AFT	18.5 ± 1.8	35.2078	−106.4557	2,726	1,025
81SAN5	10	AHe	15.9 ± 0.5	35.2078	−106.4557	2,726	1,025
81SAN6	9 & 10	AFT	19.2 ± 1.8	35.2093	−106.4607	2,616	766
81SAN6	10	AHe	18.5 ± 1.3	35.2093	−106.4607	2,616	766
81SAN7	9 & 10	AFT	18.9 ± 2.0	35.2108	−106.4643	2,549	590

Table 3
(continued)

Sample name	Ref.	Analysis method	Mean age ± error	Latitude	Longitude	Original elev. (m)	Fault dist. (m)
81SAN7	10	AHe	12.9 ± 0.9	35.2108	−106.4643	2,549	590
81SAN8	9 & 10	AFT	16.9 ± 1.8	35.2113	−106.4678	2,439	378
81SAN8	10	AHe	13.9 ± 0.5	35.2113	−106.4678	2,439	378
81SAN9	9 & 10	AFT	16.3 ± 1.8	35.2138	−106.4733	2,354	128
81SAN9	10	AHe	12.9 ± 1.3	35.2138	−106.4733	2,354	128
81SAN10	9 & 10	AFT	17.4 ± 1.8	35.2132	−106.4747	2,262	0
81SAN10	10	AHe	14.5 ± 1.5	35.2132	−106.4747	2,262	0
Ladron Peak transect; Loma Pelada fault (70°E); southern Albuquerque Basin, southern RGR							
88LAD01	5	AFT	12.0 ± 1.2	34.4238	−107.0390	1,866	357
88LAD02	5	AFT	10.6 ± 1.5	34.4242	−107.0500	1,927	760
88LAD03	5	AFT	10.0 ± 1.1	34.4258	−107.0563	2,012	1,038
88LAD04	5	AFT	11.2 ± 1.5	34.4313	−107.0807	2,574	2,364
88LAD05	5	AFT	13.4 ± 1.8	34.4282	−107.0765	2,439	2,071
88LAD06	5	AFT	14.1 ± 2.0	34.4275	−107.0288	1,829	0
88LAD08	5	AFT	32.2 ± 11.9	34.4403	−107.0925	2,476	2,599
88LAD11	5	AFT	29.1 ± 10.1	34.4338	−107.0850	2,796	2,669
TM(88LAD06)	11	AHe	12.4 ± 0.3	34.4275	−107.0288	1,829	0
Polvadera Mountain transect; Socorro Canyon fault (60°E); southern Albuquerque Basin, southern RGR							
90LEM01	5	AFT	12.5 ± 2.0	34.1802	−106.9895	1,957	493
90LEM02	5	AFT	8.0 ± 1.8	34.1823	−106.9865	1,982	374
90LEM03	5	AFT	6.7 ± 1.7	34.1808	−106.9855	1,902	260
90LEM04	5	AFT	8.6 ± 1.8	34.1795	−106.9815	1,823	9
90LEM05	5	AFT	6.1 ± 1.7	34.1978	−106.9898	1,921	458
90LEM06	5	AFT	6.4 ± 1.7	34.1990	−106.9830	1,847	78
90LEM07	5	AFT	6.5 ± 1.7	34.2029	−106.9830	1,762	0
North Baldy transect; La Jencia fault (80°E); southern Albuquerque Basin, southern RGR							
88MAG05	5	AFT	26.7 ± 6.2	34.0732	−107.1613	2,195	424
88MAG06	5	AFT	16.1 ± 4.4	34.0773	−107.1513	2,109	211
88MAG07	5	AFT	16.9 ± 7.8	34.0767	−107.1422	2,055	11
88MAG09	5	AFT	31.3 ± 11.0	34.0577	−107.1785	2,988	1,520
88MAG10	5	AFT	46.5 ± 8.4	34.0578	−107.1778	2,963	1,485
88MAG11	5	AFT	9.6 ± 1.6	34.0613	−107.1722	2,695	1,118
88MAG12	5	AFT	13.4 ± 3.5	34.0623	−107.1715	2,695	1,129
88MAG13	5	AFT	19.1 ± 4.6	34.0643	−107.1663	2,591	934
88MAG14	5	AFT	18.7 ± 4.7	34.0663	−107.1622	2,530	804
88MAG15	5	AFT	15.6 ± 2.9	34.0717	−107.1487	2,366	458
88MAG16	5	AFT	11.7 ± 3.3	34.0755	−107.1452	2,226	228
88MAG17	5	AFT	5.3 ± 2.4	34.0757	−107.1493	2,104	175
88MAG18	5	AFT	4.6 ± 2.3	34.0808	−107.1437	2,061	40
17NB	TS	ZHe	14.4 ± 0.6	34.0764	−107.1419	2,048	0

elev. = elevation; Fault dist. = fault parallel distance; TS = This study; AHe = apatite (U-Th)/He; AFT = apatite fission track; ZHe = zircon (U-Th)/He; Ref. = citation; (1) Landman & Flowers, 2013; (2) Naeser et al., 2002; (3) Abbey & Niemi, 2018; (4) Bryant & Naeser, 1980; (5) Kelley et al., 1992; (6) Ricketts et al., 2016 (7) Shannon, 1988; (8) Lindsey et al., 1986; (9) Kelley & Duncan, 1986; (10) House et al., 2003; (11) Ricketts et al., 2015.

The northernmost transect in the UAR Basin that records exhumation is the Mount Elbert transect, composed of AHe and AFT data (Bryant & Naeser, 1980; and Abbey & Niemi, 2018; Table 3). Exhumation on the Mount Elbert transect is observed from ~3-km depth at a rate of ~0.4 mm/yr from ~7 Ma to present (Figure 5).

4.1.3.3. Blue River Basin

In the Blue River Basin, which is the northernmost asymmetric rift basin in the RGR, we identified two vertical transects in the southern part of the Gore Range (Table 3). The Buffalo Mountain transect consists of AFT data (Naeser et al., 2002) and reveals heating, possibly by burial at ~14 Ma followed by rapid exhumation from ~4-km depth at a rate of ~0.5 mm/yr beginning ~10 Ma and slowing to a rate of ~0.3–0.4 mm/yr from 7 Ma to the present (Figure 5).

The Keller Mountain transect includes AHe and AFT data (Naeser et al., 2002; and Landman & Flowers, 2013; Table 3) and chronicles exhumation from 18 to 15 Ma at a rate of ~1.3 mm/yr. The thermal history model also uncovers a pulse of exhumation from 2 to 0 Ma at a rate of ~1.0 mm/yr. The total magnitude of exhumation recorded by the Keller Mountain transect is >6 km (Figure 5).

4.2. Summary of Low-Temperature Thermochronometry Data and Inverse Modeling

In the southern RGR fault, initiation occurs at ca. 25 Ma on at least one fault segment (North Baldy transect). Other fault segments in the southern RGR record rapid exhumation occurring at different times and rates, with faults typically being active for several million years at a time, starting between 20 and 12 Ma and continuing to the present (Figure 3). In the central RGR, the majority of the cooling recorded is prior to rift initiation, with the exception of the southernmost transect (Sandia Mountains), which records fault initiation at ca. 25 Ma (Figure 4). In the northern RGR, numerous fault segments initiate at ca. 25 Ma; however, other individual fault segments progressively initiate over the following 10 Myr, and several fault segments show a renewed exhumation pulse post-5 Ma (Figure 5).

In summary, there are fault segments within the RGR that initiated at ca. 25 Ma throughout the entire rift. Exhumation rates during the early phase of faulting are higher in the northern RGR (~0.4 to 0.6 mm/yr), compared to the southern RGR (~0.3 mm/yr; Figures 3 and 5). Fault initiation, growth, and linkage appears to be a progressive process in the RGR, with additional fault segments initiating throughout the middle Miocene. This progressive, and protracted, onset of faulting is consistent with high-density thermochronometric studies (Abbey & Niemi, 2018), as well as with detailed structural studies (Liu et al., 2019) in northern RGR. As additional fault segments initiated between ca. 18 and 10 Ma throughout the RGR, many faults record faster exhumation rates (~0.5 to ~1.3 mm/yr; Figures 3–5). We find that faulting initiated fairly contemporaneously along the rift and that exhumation rates increased as new segments initiated and most-likely linked together (Abbey & Niemi, 2018). Understanding these faulting stages helps to differentiate between rift models and reveals that a northward propagating model is not well supported by evidence for the initiation of faulting from thermochronometric data along the RGR. To further discriminate between rift models, we next compare the spatial and temporal relationships between the rift-related faulting and rift-related magmatism.

5. RGR Magmatism

Volcanic activity within rifts is commonly localized along major boundary faults, transfer zones, and limited portions of rift shoulders (i.e. off-axis volcanism) (Corti, 2012). Magmatism often assists with rifting and helps to transfer strain through ACZs (e.g., Busby, 2013; Rowland et al., 2007, 2010) by dike injection (Rowland et al., 2010; Stahl & Niemi, 2017). Volcanism in continental rift zones, grabens, and other manifestations of extensional tectonism is commonly dominated by mafic alkaline compositions (indicating an asthenospheric source) or has a bimodal composition, in which case low-silica basalts and high silica rhyolites are erupted in the same location (e.g., Bailey, 1974; Cosca et al., 2014; Johnson & Thompson, 1991; Kellogg, 1999; Tweto, 1979).

5.1. Existing Interpretations of Colorado and New Mexico Volcanism

Cenozoic volcanism in Colorado and New Mexico is extensive and fairly continuous, and volcanism may not necessarily be an indicator of rift activity (Corti et al., 2019), thus using the history of volcanism to deduce the onset of rifting is challenging. Rather than using the timing of volcanism as a proxy for the onset of rifting, we find it is necessary to try and define or extract a particular signal from the nearly continuous Cenozoic volcanism to identify "rift-related" magmatism. Previous studies suggest that rift-related magmatism in the RGR began between 29 and 26 Ma, when the style and chemical signature of volcanism changed from intermediate andesitic ignimbrites to eruptions of alkaline basalt and bimodal lava compositions in Colorado and New Mexico (Chapin et al., 2004; Epis & Chapin, 1974; Lindsey et al., 1983; Lipman & Mehnert, 1975; Miggins et al., 2002; Tweto, 1979). This transition is proposed to be associated with slab-rollback, retreat, or detachment of the Farallon slab and subsequent development of the RGR (Cosca et al., 2014; Ricketts et al., 2015). However, most of the Cenozoic volcanic rocks in Colorado and New Mexico erupted outside the boundaries of the present-day rift. We therefore reassess spatiotemporal patterns

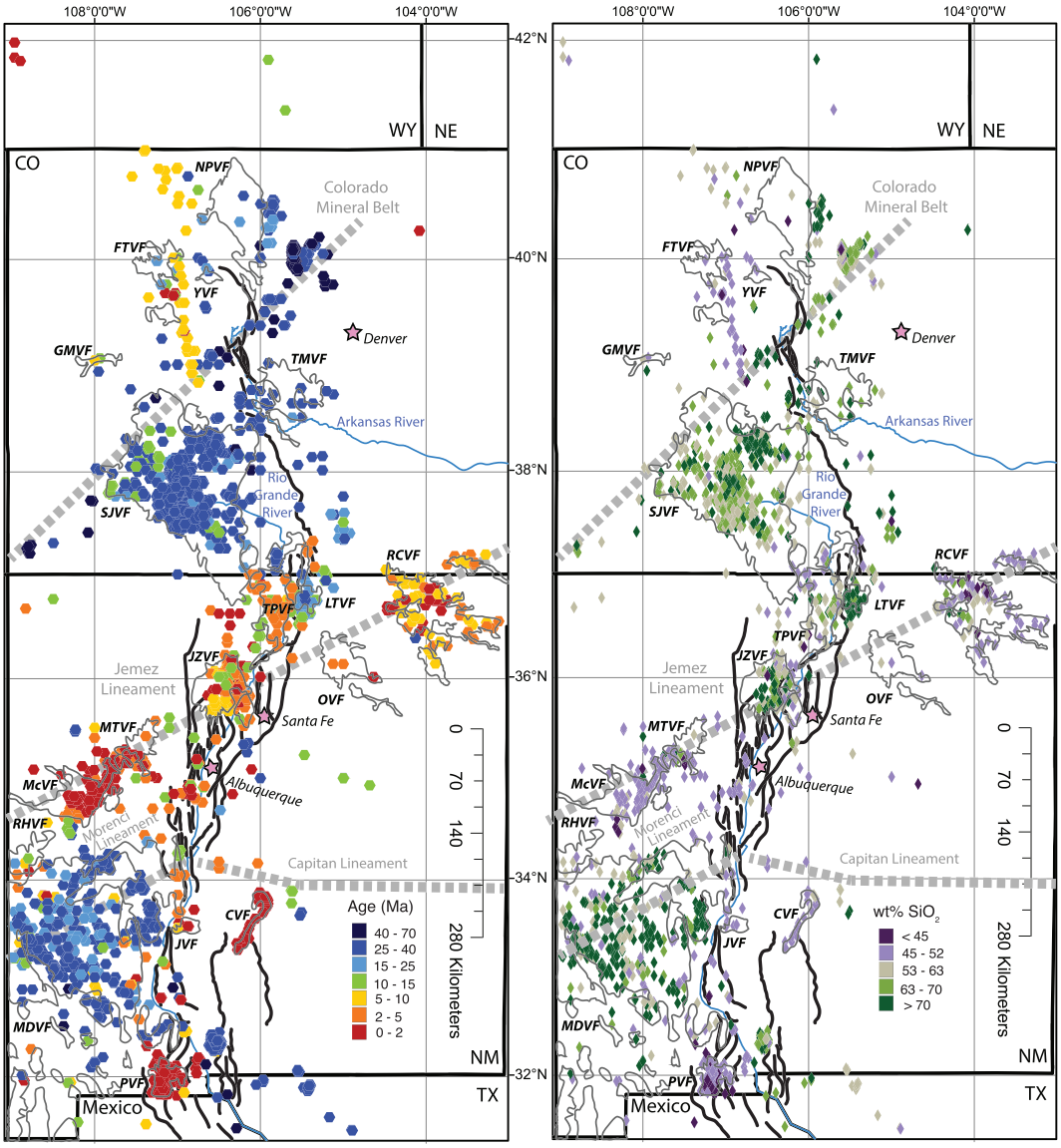

Figure 6. Age and SiO_2 content for Cenozoic volcanic deposits in Colorado and New Mexico from EarthChem database (see text and Table 4 for information on search query). Major lineaments indicated by dashed gray lines and large-scale volcanic-fields named with the following abbreviations: PVF = Potrillo volcanic field; MDVF = Mogollon-Datil volcanic field; JVF = Jornada volcanic field; CVF = Carrizozo volcanic field; RHVF = Red Hills volcanic field; McVF = McCarty's volcanic field; MTVF = Mount Taylor volcanic field; JZVF = Jemez volcanic field; TPVF = Taos Plateau volcanic field; OVF = Ocate volcanic field; LTVF = Latir volcanic field; RCVF = Raton-Clayton volcanic field; SJVF = San Juan volcanic field; TMVF = Thirty-nine Mile volcanic field; GMVF = Grande Mesa volcanic field; YVF = Yarmony volcanic field; FTVF = Flat Tops volcanic field; NPVF = North Park volcanic field.

in volcanic ages and chemical compositions to determine what role magmatism has played in accommodating extension within the RGR.

5.2. Compilation of the RGR Volcanic Data

We revisit the spatial, compositional, and temporal evolution of magmatism in the greater RGR region using databases of volcanic rock information (EarthChem; http://www.earthchem.org/portal; accessed February 2018). We compiled chemical and age data related to all volcanic rocks in NM and CO with ages from 70 to 0 Ma (Table 4; more details on data compilation and filtering in supporting information).

To evaluate the hypothesis that rift-related volcanism began with a bimodal alkaline signal at ~29–26 Ma, we filter the information from EarthChem (Table 4; more details on data compilation and filtering in supporting information) and map the spatial extent of volcanism at several key time periods (Figure 6). We also plot the frequency of lava composition as a function of time using major oxide composition data to discriminate

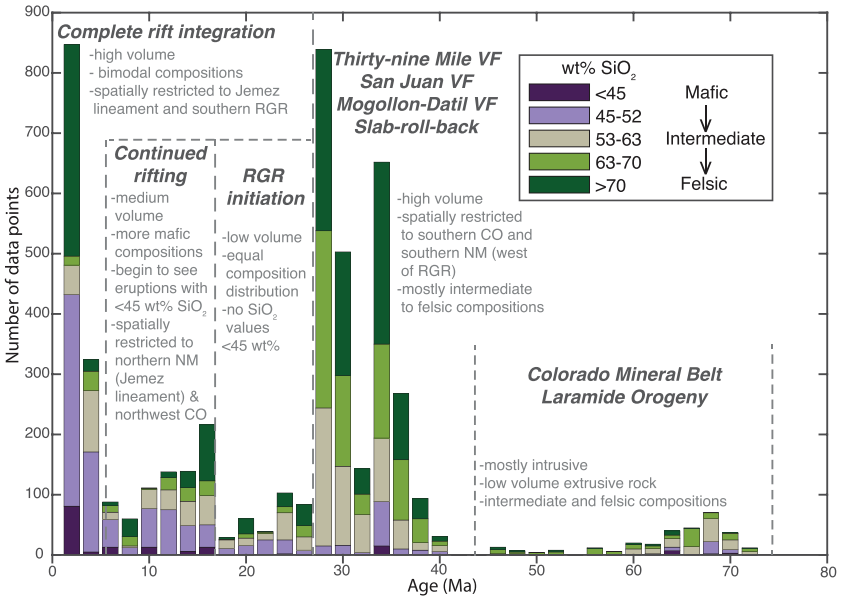

Figure 7. Stacked histogram with age and SiO data for volcanic points gathered from EarthChem database (see text, Table 4, and supporting information for information on search query). Note that this is all data published in EarthChem with no filter to single out each specific flow event, and the number of points for each age bin is not directly related to volume of magmatism.

between prerift and synrift volcanic rocks (Figures 7 and S3). Major oxide data are more prevalent across the RGR than trace element or isotopic data, and thus, we use the oxide compositional signature as a way to assess alkalinity of erupted volcanic rocks. Plotting these data on a Harker diagram of SiO_2 versus Na_2O and K_2O, we find that there is no obvious temporal trend in the alkalinity signature of the Cenozoic volcanic rocks in CO and NM (Figure S3). However, there is temporal variation in the wt% of SiO_2 seen in the volcanic rocks. We therefore assess the use of SiO_2 as a simple discriminant for a transition in eruption composition. We focus on lava "compositions" as defined by the wt% of SiO_2 (e.g., <45% SiO_2, 45–52%, 53–63%, 63–70%, and >70%; Figures 6, 7, and S3).

5.3. Spatial and Compositional Evolution of Volcanism in the RGR Region

The oldest volcanism in our compilation spans from 70 to 40 Ma and is characterized by volcanic rocks of almost entirely intermediate to felsic compositions (>53% SiO_2; Figure 7). Magmatism at that time was associated with the Laramide Orogeny and most of what is preserved is plutons, stocks, and plugs, with limited preservation of volcanic rock. The spatial extent of these rocks is limited to the Colorado Mineral Belt lineament in central CO, a southern belt in NM (Ortiz Mountains and Mogollon-Datil volcanic fields), and in west Texas along the TX and Mexico border (Figure 6). From 40 to 27 Ma, volcanic rocks are dominated by intermediate and felsic ignimbrites (>53% SiO_2; Figure 7) that form several large volcanic fields (VFs) outside the bounds (mostly west) of the present-day rift in both CO and NM (Thirty-nine Mile VF, San Juan VF, and Mogollon-Datil VF; Figures 6 and 7; e.g., Chapin et al., 2004). Between ~27 and ~21 Ma, volcanism occurs almost exclusively via intermediate and rhyolitic eruptions in the Mogollon-Datil VF in southwestern New Mexico (Figure 6; Chapin et al., 2004). In summary, late Eocene to Oligocene volcanism is intermediate to felsic in composition, is located, for the most part, west of the present-day RGR, and is attributed to slab foundering and rollback followed by mantle upwelling (Chapin et al., 2004; McMillan et al., 2000; Ricketts et al., 2015).

Throughout the early Miocene (~21–15 Ma), there is a lull in volcanism with only a few small-volume felsic to intermediate eruptions scattered around the Mogollon-Datil VF, San Juan VF, and Latir VF (Figure 6). Renewed volcanism initiates in the middle Miocene (~15 Ma) and, for the first time, is spatially associated with the present-day extent of the RGR. During this phase of volcanism, mafic (<52% SiO_2) compositions become more prevalent (subequal quantities of mafic, intermediate, and felsic lavas; Figure 7; Chapin

Table 4
EarthChem Portal Search Query

Location (box defined by coordinates)	42°N; 30°N; 109°W; 103°W
Age (Ma)	0 to 70
Rock type	All categories within the EarthChem categories of Igneous > volcanic
Results (source and number of reported samples)	NAVDAT: 3984 GEOROC: 1741 USGS: 1685 Total: 7410

et al., 2004). Magmatism is focused in the central RGR in the Jemez, Taos, and Latir volcanic fields as well as some minor eruptions in the southern Albuquerque Basin (Figures 6 and 8). By ca. 10 Ma, the prevalence of mafic volcanism increases, and eruptions occur primarily along the Jemez lineament in the Raton, Taos, and Jemez VFs until ~2 Ma (Figure 6). Minor late Miocene eruptions also occur in northwest CO in the Yampa VF at this time (Figure 6; Cosca et al., 2014). From 2 Ma to present, volcanic eruptions are primarily mafic in composition and erupt along the Jemez Lineament in the McCarty's, Mount Taylor, Ocate, and Raton-Clayton volcanic fields (Figures 6 and 7). The Jemez VF is also active at this time, with eruptions of both basalt and rhyolite (i.e., Bandelier tuff; Chapin et al., 2004). Volcanic activity begins in the southern RGR after 2 Ma, with the eruption of low silica (<45 wt%) volcanic rock in the Jornada del Muerto, Carrizozo, and Potrillo VFs (Figures 6 and 7).

The spatiotemporal patterns of dominantly intermediate to felsic compositions peripheral to the present-day RGR boundary and erupted prior to 21 Ma are markedly unlike the pattern of mafic eruptions that have occurred since ~15 Ma and which are located along the northeast-southwest trending Jemez lineament, crossing the central RGR (Figure 6). Through this reanalysis, we are unable to identify compelling evidence that supports previous suggestions that rift initiation can be documented by mafic and bimodal magmatism during the Oligocene (Chapin et al., 2004; Epis & Chapin, 1974; Lindsey et al., 1983; Lipman & Mehnert, 1975; Miggins et al., 2002; Tweto, 1979). Instead, voluminous mafic and bimodal eruptions within the RGR begin in the middle Miocene, roughly 10 Myr after fault initiation as determined by our thermochronometry analysis.

6. Discussion

Our analysis of low-temperature thermochronometry data, interpretation of modeled fault-block thermal histories, and evaluation of spatiotemporal patterns of Cenozoic magmatism provides the means to assess rift development and mechanisms of extensional accommodation using a consistent approach throughout the entire extent of the RGR. We use these data to (1) document the rift-wide onset of faulting as well as the processes of fault segment growth and linkage throughout the RGR. With this information, we are able to (2) evaluate rift propagation models and further our analysis by combining faulting information with our reanalysis of regional magmatism to resolve spatial patterns in the mechanisms of extensional accommodation along the RGR. Hence, we are poised to ask the question of (3) whether along-rift changes in physiography are the product of evolutionary stages, extension accommodation mechanisms, weakness from previous deformation events, characteristics of the crust and lithosphere beneath the surface of the rift, or some combination of these factors.

6.1. Initiation, Growth, and Integration of the RGR System

Here we use our complied and modeled thermochronometry data in combination with our summary of regional Cenozoic magmatism to address the development, growth, and integration of the RGR.

6.1.1. Thermochronometric Constraints on Spatial and Temporal Patterns of Rift-Related Fault Initiation and Growth

To understand fault growth and rift basin connection in the RGR, we have taken an approach similar to that presented by Abbey and Niemi (2018) who showed that a multi-transect approach is a viable method for identifying rift initiation and quantifying fault growth patterns. Their work focused on vertical transects

10.1029/2019TC005635

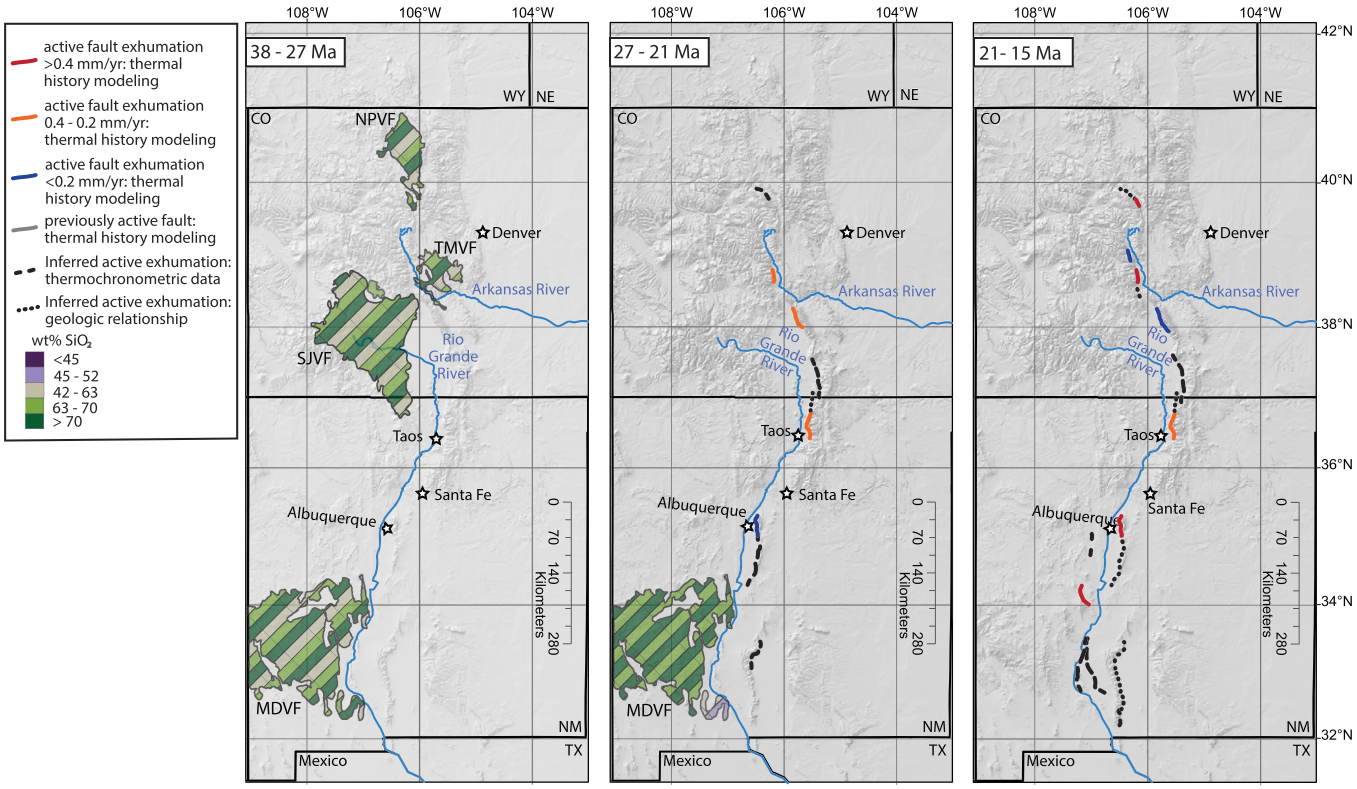

Figure 8a. Evolution of faulting and magmatism along the Rio Grande rift presented in time steps. Faults patterned based on data source (i.e., inferred from geologic relationships [dotted], inferred from cooling ages not used in thermal history models [dashed], and from inverse thermal history modeling [solid: colored by rate of exhumation]). Schematic versions of the active volcanic fields in each time step are colored to represent general eruption compositions and named with the following abbreviations: MDVF = Mogollon-Datil volcanic field; SJVF = San Juan volcanic field; TMVF = Thirty-nine Mile volcanic field; NPVF = North Park volcanic field. Note that although Figure 8 shows some data for volcanism between 21 and 15 Ma, the amount is too small to appear on the 21–15 Ma panel here.

from the UAR Basin, which documented phases of segment initiation occurring at ~25 and ~18 Ma, and fault exhumation acceleration, which was inferred to be related to fault growth via tip propagation and segment linkage (Curry et al., 2016; Kim & Sanderson, 2005), a process which appears to occur over a span of several millions of years (Abbey & Niemi, 2018).

Fault initiation along the length of the entire RGR occurred at ~25 Ma in a number of transects, similar to the onset of exhumation observed from the densely sampled UAR Basin (Abbey & Niemi, 2018). Other transects throughout the RGR record a later onset of exhumation, which we infer to reflect individual fault segment initiation and growth (Figure 9). Rift-wide, we observe an increase in the rate of exhumation in the middle to late Miocene, similar to the timing of exhumation rate increase observed in the UAR Basin (Abbey & Niemi, 2018), and the subsidence records from the central rift basins (van Wijk et al., 2018). Interpretation of the inverse thermal history models of the thermochronometric data suggests that each of the rift basins, with the exception of the Española Basin in the central RGR, developed through a process of fault segment initiation followed by tip growth and linkage over the course of 10 to 15 Myr, similar to the pattern observed in the UAR basin where the density of thermochronometric data is greatest (Figures 8 and 9). Thus, by ~15 to 10 Ma, fault segments within each individual rift basin became linked, forming the main basin-bounding faults we observe today. Once linked, the rift-bounding faults continued to grow, and by ~10–5 Ma, individual basins began to connect via ACZs (Figures 3–5 and 9).

ACZs aid in strain transfer and basin integration in different ways throughout the RGR. For example, the Poncha Pass ACZ transfers strain between the San Luis Basin and the UAR Basin along a narrow region of northeast-southwest striking faults which developed in the late Miocene (Hubbard et al., 2001; Kellogg

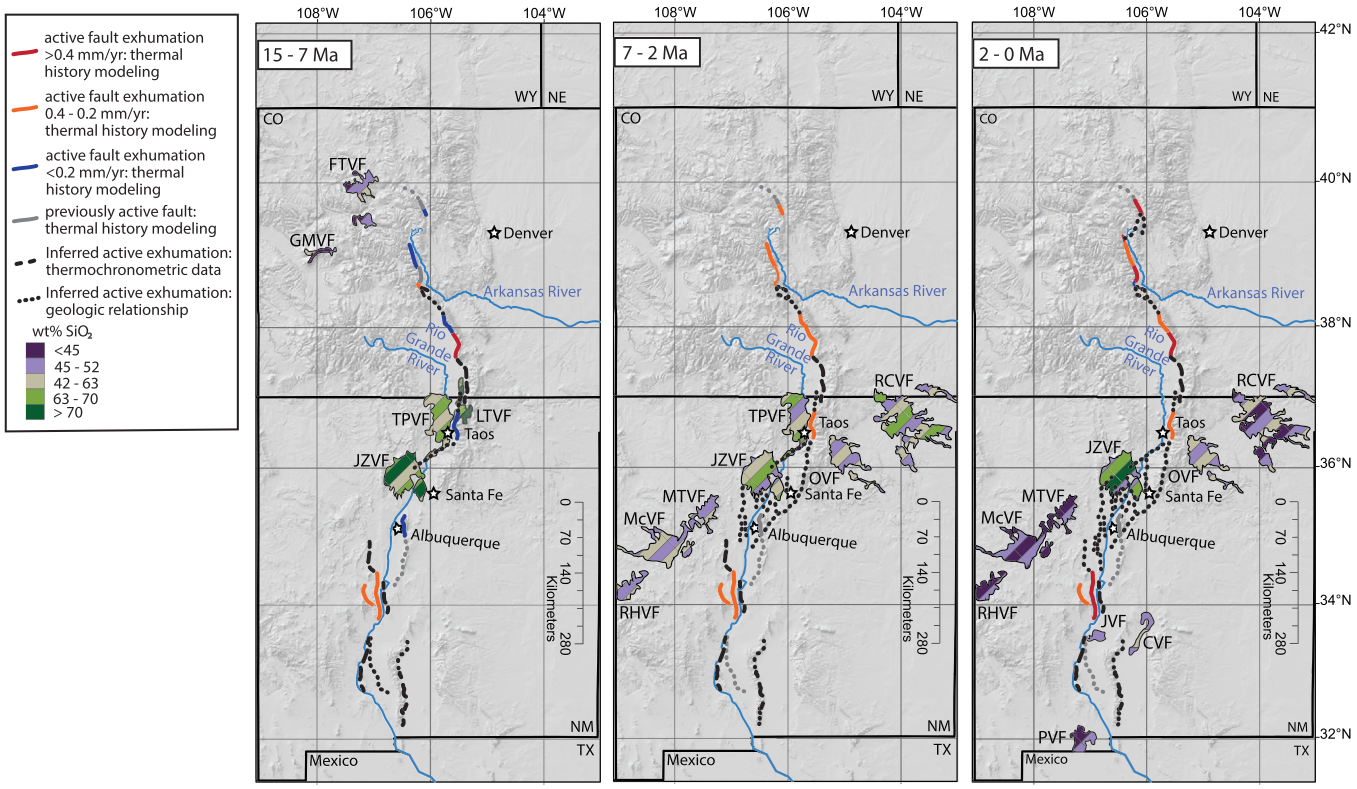

Figure 8. *(continued)*

et al., 2017; Minor et al., 2019). In the central and southern RGR, strain transfer is more commonly accommodated via magmatic injection (e.g., Casey et al., 2006; Keir et al., 2006) and across broad areas of overlapping faults that gradually transfer displacement (e.g., Lewis & Baldridge, 1994; Figure 9). For example, the Tijeras, Santa Ana, and Embudo ACZs in the central RGR are associated with voluminous volcanism, numerous strike-slip faults, and a concentration of intrabasin faults that began accommodating oblique slip and strain transfer in the middle Miocene (e.g., Figure 9; Grauch et al., 2017). In contrast to the central RGR ACZs, which contain notable surface faults and eruptive volcanism, the Cutter Sag transfer zone and Socorro ACZ in the southern RGR exist in a region with little to no fault expression or volcanism at the surface but evidence for large subsurface magmatism (e.g., Figure 9; Sanford et al., 1977; Mack & Seager, 1995; Balch et al., 1997).

The fault initiation, growth, and linkage patterns we observe from our new thermal history modeling reveal a framework in which individual fault segments link to become large-basin-bounding faults. Each basin-bounding fault then continues to develop by transferring strain across ACZs, frequently with the help of magmatic injection.

6.1.2. Strain Transfer and Basin Connection Through Magmatically Driven ACZs

Magmatism within the RGR is almost exclusively found in the central part of the rift. Eruptive magmatism, however, is not present in the central RGR until the middle Miocene, and the lack of regional magmatism suggests that the onset of magmatism cannot be used as an indicator for whole rift initiation, although it is a potentially useful indicator for understanding spatial variability in the mechanisms of extensional accommodation. The lack of thermochronometric ages <30 Ma in the central RGR suggests minimal displacement on surface-breaking normal faults in the central RGR (Figure 4; Kelley, 1990), and the evidence that seismicity in this region is associated with the major magmatic centers rather than the large strike-slip faults (Nakai et al., 2017) indicates that the connection between the northern and southern RGR is accommodated predominantly by magma injection processes rather than tectonic processes (Figures 4, 9, and 10; Kelson et al., 2004; Grauch et al., 2017). Therefore, the central part of the rift appears to be the sole region where rifting is primarily accommodated by magmatism. The timing of eruptive magmatism in the central RGR

10.1029/2019TC005635

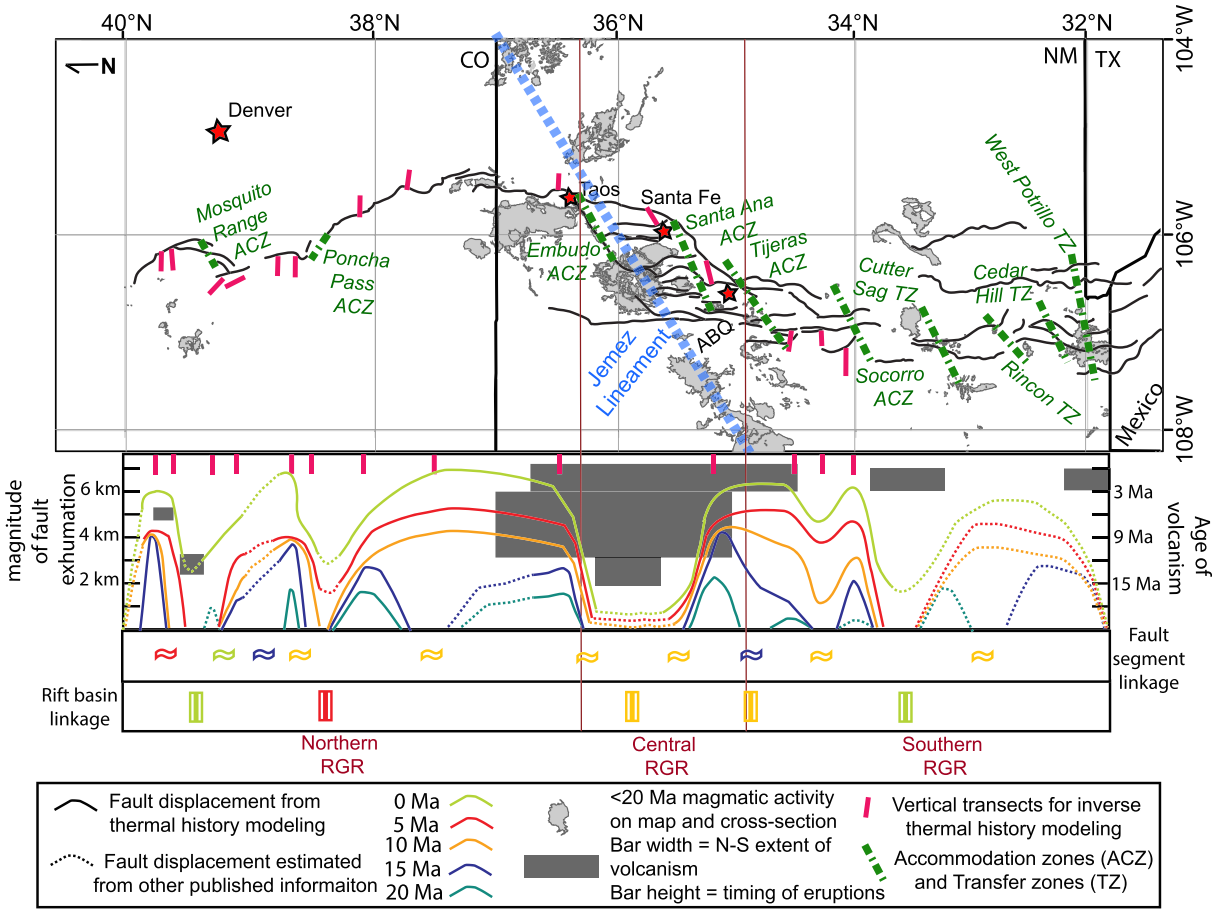

Figure 9. Fault displacement and growth patterns integrated with middle to late Cenozoic magmatism showing linkage of fault segments and rift basins from rift initiation at ~25 Ma to present. Map (top) displays rift faults (solid black lines) <20 Ma volcanic fields (gray polygons), accommodation and transfer zones (green dashed lines; Chapin & Cather, 1994; Mack & Seager, 1995; Abbey & Niemi, 2018), Jemez Lineament (blue dashed line), and locations for vertical transects used for thermal history modeling in this study (pink bars) (Table 3 and Figures 3–5). Cross section (bottom) presents fault displacement timing and magnitudes as determined from thermal history modeling (solid curves) and other published information including thermochronometric data and offset stratigraphy with known depositional ages (Figures 3–5 and Table 1). The <20 Ma magmatic activity on Jemez Lineament and other minor volcanic fields is shown in gray bars indicating eruption timing (*y* axis and height) and north-south spatial extent (*x* axis aligned with map above). ABQ = Albuquerque; ACZ = accommodation zone; TZ = transfer zone.

coincides with an increase in exhumation rates rift-wide and may reflect the development of magmatic-dominated ACZs connecting basins from the northern RGR (San Luis Basin) to the southern RGR (Albuquerque Basin).

Volcanism within the bounds of the rift also occurs in the southern RGR, where basaltic eruptions have occurred post-2 Ma (Figures 6, 8, and 9). Minor, low-silica basaltic eruptions are common in extensional settings such as Death Valley (e.g., Manley et al., 2000) and Lunar Crater (e.g., Scott & Trask, 1971; Valentine & Cortés, 2013) in the Basin and Range, and in the southern RGR, this magmatism appears to play a role in transferring strain through dike injection into established ACZs in the southern RGR (Figure 9; Mack & Seager, 1995). We hypothesize that the majority of the extension in the southern RGR is accommodated via faulting on the large interconnected north-south striking basin-bounding normal faults where thermochronometric cooling ages range from ~20 to 5 Ma (Figure 3; Kelley & Chapin, 1997) and that integration between the Albuquerque Basin and southernmost RGR basins occurs through magmatism within the southern accommodation and transfer zones, as evidenced by the active eruptive centers, subsurface magma bodies, and seismicity related to dike injection (e.g., Balch et al., 1997; Nakai et al., 2017; Sanford et al., 1977) (Figure 9). Therefore, we suggest that although rift initiation was mainly tectonically driven, integration of the whole rift system was magma assisted.

6.1.3. Summary of RGR Growth and Integration of Rift Basins

The integration and accommodation of the entire RGR occured through a combination of both faulting and magmatism. As faults and basins grew and linked in the northern and southern RGR through the middle Miocene, rifting was accommodated through magmatic injection in the central RGR (Figures 6–9). Linking between individual basins began in the middle Miocene, connecting the San Luis Basin, Española Basin, and Albuquerque Basin through active magmatism (Figures 8 and 9). In the northern and southern RGR basins, linkage occurs in the late Miocene, with linkage in the north occurring from continued growth of basin-bounding faults and linkage in the south from a combination of fault growth and minor Quaternary volcanism (Figures 8 and 9). We can document this in the slowly evolving RGR and find that fault segment linkage within a single basin can take 10–15 Myr after fault initiation and that integration between basins can take another 5–10 Myr to fully develop. Thus, even though several parts of the rift initiated synchronously and sections of the rift have been actively accommodating extension since ca. 25 Ma, the development of a fully integrated system of connected rift basins did not occur until ~5 Ma (Figures 8 and 9).

6.2. Controls on Rift Physiography From Inherited Structures and Lithospheric Architecture

Observed differences in physiography and accommodation style in continental rifts globally are not reflective of a continuum of rift evolutionary stages but rather must be related to other factors that influence extensional processes, such as inherited crustal weaknesses and/or lithospheric architecture (Brun, 1999; Buck, 1991; Corti, 2012; Corti et al., 2018; Fletcher et al., 2018). Significant differences in lithospheric thickness exist throughout much of the western United States and around the Colorado Plateau (e.g., Levander et al., 2011). Within the RGR, the depth to the lithosphere-asthenosphere boundary (LAB) shallows from >100 km beneath the Colorado Plateau and northern RGR to 60–70 km beneath the Basin and Range and southern RGR (Levander et al., 2011; Figure 10).

Consequently, the northern RGR faults are rupturing a region where lithospheric thicknesses are >100 km (Levander et al., 2011), and the southern RGR faults are rupturing a roughly 65-km-thick lithosphere (Figure 10; Levander et al., 2011). These differences in thickness may account for differences in the styles of faulting seen in the northern and southern RGR, as wider, more diffuse rift zones are often associated with thinner and warmer underlying lithosphere as opposed to narrow, deep grabens that are found in areas with a cold, thick lithosphere (Buck, 1991; Ebinger, 2005; Ebinger et al., 1991). The step in the LAB in the central RGR also occurs along the Jemez lineament and is spatially coincident with known Proterozoic terrane boundaries (e.g., the suture between the Yavapai and Mazatzal terranes; Figure 10; Karlstrom & Bowring, 1988; Karlstrom & Humphreys, 1998; Shaw & Karlstrom, 1999; Chapin et al., 2004; Chapin, 2012). The formation of the active volcanic centers of the Jemez lineament over this LAB step suggests that inherited structure from ancient features continues to play a role in controlling deformation in the region (Baldridge et al., 2006). Similar to the RGR, changes in rift deformation style occur in the East African rift system and are coincident with “steps” in crustal thickness attributed to deep-seated Neoproterozoic sutures and other inherited weaknesses (e.g., Boone et al., 2019; Corti et al., 2019), suggesting that such controls are common in continental rift systems.

Abrupt lithospheric thickness changes not only suggest inheritance from preexisting weaknesses caused by previous deformation events but also appear to have strong controls on the localization of magmatism (e.g., Corti et al., 2019). Beyond the recognized extent of the RGR, large volcanic eruptions occur along the entire length of the Jemez lineament and around the Colorado Plateau at the transition between the plateau and the Basin and Range. An abrupt change in lithospheric thickness is most prominent along this transition (Figure 10), and others have recognized such steps in lithospheric thickness can be a mechanism for driving magmatism, for example, through edge-driven convection (e.g., van Wijk et al., 2010; Levander et al., 2011; Rudzitis et al., 2016; Figure 10).

Our estimated exhumation magnitudes and rates determined from thermal history modeling along with the localized patterns seen in Cenozoic magmatism further emphasizes the physiographic differences that exist between the southern, central, and northern RGR. Although a detailed exploration of crustal inheritance and regional preexisting structure is beyond the scope of this work, we propose that crustal and lithospheric properties (i.e., thickness and potentially age and rheology) control rift accommodation and play a role in the orientation of faulting and magmatism along the RGR, as seen in continental rifts elsewhere (Figure 10; e.g., Brun, 1999; Corti, 2012; Fletcher et al., 2018; Corti et al., 2018; Corti et al., 2019). Therefore, we suggest that

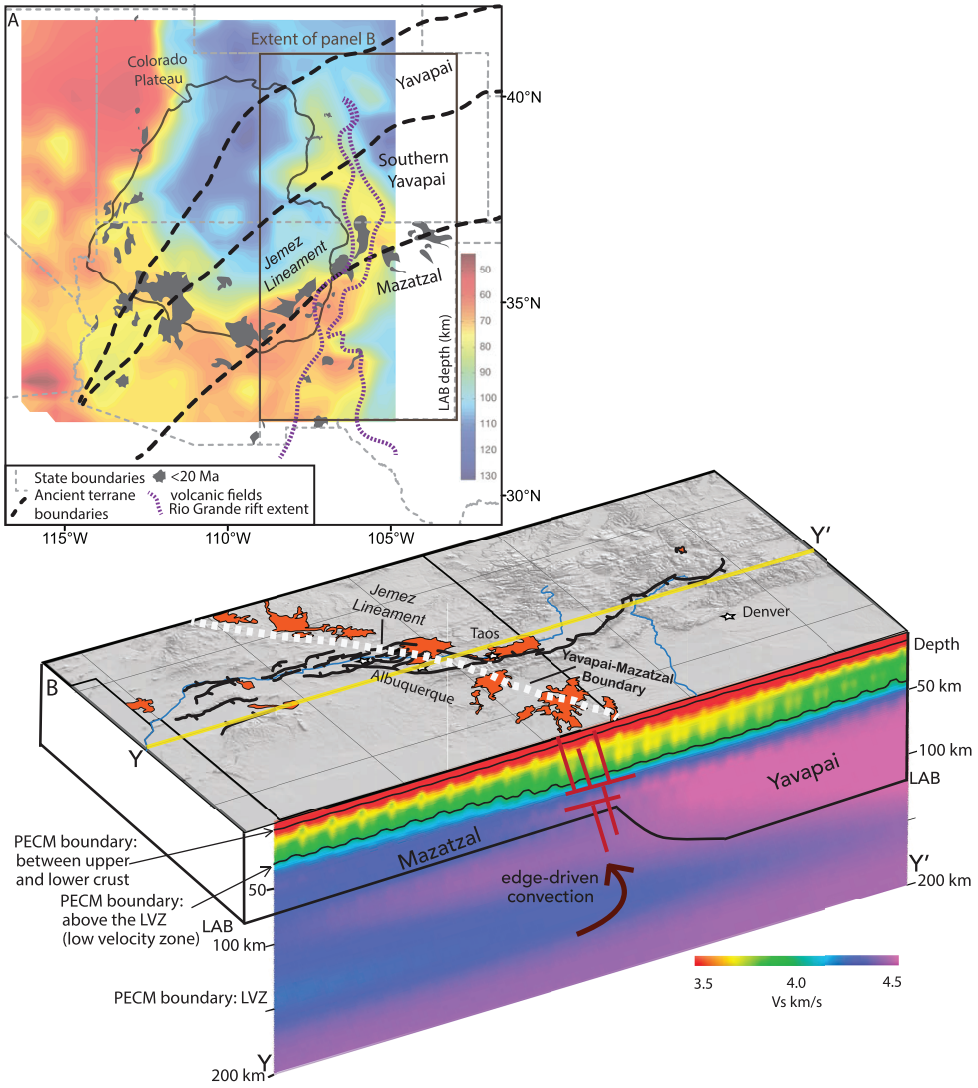

Figure 10. (a) Relationships between the RGR, volcanic fields surrounding the RGR and Colorado Plateau, and ancient terrane boundaries (Chapin et al., 2004; Karlstrom & Bowring, 1988; Karlstrom & Humphreys, 1998; Shaw & Karlstrom, 1999). Background image produced by Levander et al. (2011) shows the average lithosphere-asthenosphere boundary (LAB) depth determined from USArray Ps and Sp receiver functions and Rayleigh wave tomography. Note that the "rift-related" volcanism along the Jemez lineament and oblique to the strike of the rift is spatially coincident with the Yavapai-Mazatzal terrane boundary where there is a large "step" in lithospheric thickness. This is similar to the "step" seen around much of the Colorado Plateau where volcanism of comparable age and chemical composition occurs. (b) Block diagram showing simplified Quaternary faults in the RGR (Machette et al., 1998) and volcanic fields <20 Ma in CO and NM. The depth profile colors are Vs speeds in km/s from the WUS-CAMHI-2015 model obtained through IRIS (http://ds.iris.edu/dms/products/emc/gcross-section.html) (Chai et al., 2015). Note the lithospheric thickness difference beneath the northern and southern parts of the RGR. Black line denoting the LAB is drawn at depths taken from estimates by Levander et al. (2011) (panela). The majority of the volcanism occurs along the Jemez lineament above the "step" in lithospheric thickness (Levander et al., 2011), which may be aided by edge-driven convection (Rudzitis et al., 2016; van Wijk et al., 2010).

differences in rift accommodation mechanisms (i.e., faulting vs. magmatism) are likely controlled by deep-seated lithospheric-scale properties and architecture, rather than progressive stages of rift development (e.g., Corti, 2012).

We hypothesize that preexisting structures from ancient terranes, such as the suture between the Yavapai and Mazatzal terranes, influence faulting style within the RGR (i.e., single-basin-bounding faults at a given latitude, strike-slip faults and intra-basin faults, and several basin-bounding faults at a given latitude) and encourage the localization of magmatic accommodation (i.e., through edge-driven convection along the Jemez lineament). Hence, RGR accommodation mechanisms and styles of deformation seem to be highly spatially controlled by preexisting weaknesses *and* lithospheric structure as opposed to a temporal evolution of deformation from south to north.

6.3. RGR model

Our analysis of thermochronometric data and magmatism patterns within the RGR rules out rift models involving time progressive propagation of rifting (northward propagation in the case of the RGR). Accordingly, we consider generalized synchronous rifting models—block rotation and oblique strain, as possible mechanisms driving the development of the RGR (Figure 1; e.g., Ebinger et al., 1984; Nelson et al., 1992; Brune et al., 2017; Molnar et al., 2017; Brune et al., 2018).

The greater magnitudes of horizontal extension in the southern RGR as compared to the northern RGR and the thermochronometric evidence for synchronous faulting in both regions are consistent with a block rotation model. In fact, paleomagnetic and geodetic studies argue for clockwise rotation of the Colorado Plateau, also supporting a block rotation model for RGR opening (Brown & Golombek, 1986; Chapin & Cather, 1994; Cordell, 1982; Golombek et al., 1983; Hamilton, 1981; Kelley, 1979; Kreemer et al., 2010; Lewis & Baldridge, 1994; McCall & Kodama, 2014; Zoback & Thompson, 1978). However, this rotation is suggested to have occurred in the middle to late Miocene (i.e., 10–15 Myr after rift initiation as determined by our thermochronometric data analysis). Therefore, we cannot rule out an oblique strain model especially in light of a recent global rifting study which showed that the majority of rifting is accomplished from oblique strain (Brune et al., 2018). We suggest that rifting is driven by a combination of oblique strain and block rotation, mechanisms which evolve with the changing far-field plate boundary conditions through time. Our hybrid rift model entails that rifting began in a style similar to an oblique strain model (Figure 1), with initiation in both the northern and southern RGR, followed by a linkage across a weak zone (the Jemez Lineament) and then was enhanced by block rotation in the middle to late Miocene, accounting for the greater extension magnitudes in the southern RGR (Figure 1).

7. Conclusions

Assessment of spatiotemporal relationships between rift-related faulting and magmatism in the RGR suggests synchronous rift initiation at ca. 25 Ma on several separate fault segments. Fault-segment initiation, growth, and linkage continued for 10 to 15 Myr, and magmatic accommodation in the central RGR helped to fully integrate the rift into one connected system by the late Miocene. Inherited crustal and lithospheric structure appear to play a role in controlling the surface expression and extension accommodation within continental rifts (e.g., thickness). We find that understanding rift accommodation via spatiotemporal patterns in faulting and magmatism is necessary to distinguish between competing rift initiation and growth models and may be useful for discriminating between models of continental rifting processes. Per our new understanding of controls on continental rifting processes and accommodation mechanisms, we propose that components of both oblique strain and block rotation (i.e., clockwise rotation of the Colorado Plateau) drove rifting in the RGR. Here we emphasize that understanding continental rift initiation and development through assessment of the spatiotemporal relationships between both faulting and magmatism is useful for distinguishing between rifting processes and accommodation controls and can help to determine processes and factors controlling the evolution of continental rift systems around the world.

Acknowledgments
We thank K. E. Murray for assistance with sample collection and for insightful conversations about western U.S. geology. We thank Amanda Maslyn (University of Michigan) and Victor Valencia (ZirChron LLC) for assistance with sample processing and analysis. We thank S. Baldridge and an anonymous reviewer for insightful questions and comments on previous versions of this manuscript. This work was partially supported by NSF Grant EAR-1151247 (N. A. N.), as well as a Rackham graduate student research grant and a Turner Award from the Department of Earth and Environmental Sciences at the University of Michigan (A. L. A.). All new analytical data collected as part of this study are included in the manuscript and in supporting information; in addition, the data can be found in the UM Deep Blue repository (https://doi.org/10.7302/cvn3-eq83).

References

Abbey, A. L., & Niemi, N. A. (2018). Low-temperature thermochronometric constraints on fault initiation and growth in the northern Rio Grande rift, upper Arkansas River valley, Colorado, USA. *Geology*, *46*(7), 627–630. https://doi.org/10.1130/G40232.1

Abbey, A. L., Niemi, N. A., Geissman, J. W., Winkelstern, I. Z., & Heizler, M. (2017). Early Cenozoic exhumation and paleotopography in the Arkansas River valley, southern Rocky Mountains, Colorado. *Lithosphere*, *10*(2), 239–266. https://doi.org/10.1130/L673.1

Bailey, D. K. (1974). Continental rifting and alkaline magmatism. In H. Sorensen (Ed.), *The alkaline rocks* (pp. 148–159). New York: Wiley.

Balch, R. S., Hartse, H. E., Sanford, A. R., & Lin, K. (1997). A new map of the geographical extent of the Socorro mid-crustal magma body. *Bulletin of Seismological Society of America*, *87*, 174–182.

Baldridge, W. S., Ferguson, J. F., Braile, L. W., Wang, B., Eckhardt, K., Evans, D., et al. (1994). The western margin of the Rio Grande Rift in northern New Mexico: An aborted boundary? *Geological Society of America Bulletin*, *106*(12), 1538–1551. https://doi.org/10.1130/0016-7606(1994)106<1538:TWMOTR>2.3.CO;2

Baldridge, W. S., Keller, G. R., Haak, V., Wendlandt, E., Jiracek, G. R., & Olsen, K. H. (2006). *The Rio Grande rift. In Developments in geotectonics* (Vol. 25, p. 233). Elsevier.

Biehler, S., Ferguson, J., Baldridge, W. S., Jiracek, G. R., Aldern, J. L., Martinez, M., et al. (1991). A geophysical model of the Española basin, Rio Grande rift, New Mexico. *Geophysics*, *56*(3), 340–353. https://doi.org/10.1190/1.1443048

Boone, S. C., Balestrieri, M. L., Kohn, B. P., Corti, G., Gleadow, A. J. W., & Seiler, C. (2019). Tectono-thermal evolution of the Broadly Rifted Zone, Ethiopian Rift. *Tectonics*, *38*, 1070–1100. https://doi.org/10.1029/2018TC005210

Brister, B. S., & Gries, R. R. (1994). Tertiary stratigraphy and tectonic development of the Alamosa basin (northern San Luis basin), Rio Grande rift, south-central Colorado. In G. R. Keller, & S. M. Cather (Eds.), *Basins of the Rio Grande rift: Structure, stratigraphy, and tectonic setting*, *Geological Society of America Special Paper* (Vol. 291, pp. 39–58).

Brown, L. L., & Golombek, M. P. (1986). Block rotations in the Rio Grande rift, New Mexico. *Tectonics*, *5*, 423–438.

Brun, J. P. (1999). Narrow rifts versus wide rifts: Inferences for the mechanics of rifting from laboratory experiments. Philosophical Transactions of the Royale Society 138 London Series A-Mathematical. *Physical and Engineering Sciences*, *357*, 695–710.

Brune, S., Corti, G., & Ranalli, G. (2017). Controls of inherited lithospheric heterogeneity on rift linkage: Numerical and analogue models of interaction between the Kenyan and Ethiopian rifts across the Turkana depression. *Tectonics*, *36*, 1767–1786. https://doi.org/10.1002/2017TC004739

Brune, S., Williams, S. E., & Müller, R. D. (2018). Oblique rifting: The rule, not the exception. *Solid Earth*, *9*(5).

Bryant, B., & Naeser, C. W. (1980). The significance of fission-track ages of apatite in relation to the tectonic history of the Front and Sawatch Ranges, Colorado. *Geological Society of America Bulletin*, *91*, 156–164.

Buck, W. R. (1991). Modes of continental lithospheric extension. *Journal of Geophysical Research*, *96*(B12), 20161–20178.

Buck, W. R. (2004). Consequences of asthenospheric variability on continental rifting. In G. D. Karner, B. Taylor, N. W. Droscoll, & D. L. Kohlstedt (Eds.), *Rheology and deformation of the lithosphere at continental margins* (pp. 1–30). New York: Columbia University Press.

Buck, W. R. (2006). The role of magma in the development of the Afro-Arabian Rift System. *Geological Society, London, Special Publications*, *259*(1), 43–54.

Busby, C. J. (2013). Birth of a plate boundary at ca. 12 Ma in the Ancestral Cascades arc, Walker Lane belt of California and Nevada. *Geosphere*, *9*(5), 1147–1160.

Casey, M., Ebinger, C., Keir, D., Gloaguen, R., & Mohamed, F. (2006). Strain accommodation in transitional rifts: Extension by magma intrusion and faulting in Ethiopian rift magmatic segments. *Geological Society, London, Special Publications*, *259*(1), 143–163.

Chai, C., Ammon, C. J., Maceira, M., & Herrmann, R. B. (2015). Inverting interpolated receiver functions with surface wave dispersion and gravity: Application to the western US and adjacent Canada and Mexico. *Geophysical Research Letters*, *42*, 4359–4366. https://doi.org/10.1002/2015GL063733

Chapin, C. E. (2012). Origin of the Colorado mineral belt. *Geosphere*, *8*(1), 28–43.

Chapin, C. E., & Seager, W. R, (1975). Evolution of the Rio Grande rift in the Socorro and Las Cruces areas. *26th Field Conference, New Mexico Geological Society*, 297-321.

Chapin, C. E., Wilks, M., & McIntosh, W. C. (2004). Space-time patterns of late Cretaceous to present magmatism in New Mexico-comparison with Andean volcanism and potential for future volcanism. In S. M. Cather, W. C. McIntosh, & S. A. Kelley (Eds.), *Tectonics, geochronology, and volcanism in the southern Rocky Mountains and Rio Grande rift* (Vol. 160, pp. 13–40). Socorro, New Mexico: Bureau of Geology and Mineral Resources Bulletin.

Chapin, D. E., & Cather, S. M. (1994). Tectonic setting of the axial Basins of northern and central Rio Grande Rift. In G. R. Keller, & S. M. Cather (Eds.), *Basins of the Rio Grande Rift: Structure stratigraphy and tectonic setting*, *Geological Society of America Special Publication* (Vol. 291, pp. 5–25).

Contreras, J., Anders, M. H., & Scholz, C. H. (2000). Growth of a normal fault system: Observations from the Lake Malawi basin of the east African rift. *Journal of Structural Geology*, *22*(2), 159–168.

Cordell, L. (1982). Extension in the Rio Grande rift. *Journal of Geophysical Research*, *87*, 8561–8569.

Corti, G. (2008). Control of rift obliquity on the evolution and segmentation of the main Ethiopian rift. *Nature Geoscience*, *1*(4), 258.

Corti, G. (2009). Continental rift evolution: From rift initiation to incipient break-up in the Main Ethiopian Rift, East Africa. *Earth Science Reviews*, *96*, 1–53.

Corti, G. (2012). Evolution and characteristics of continental rifting: Analogue modeling-inspired view and comparison with examples from the East African Rift System. *Tectonophysics*, *522-523*, 1–33.

Corti, G., Cioni, R., Franceschini, Z., Sani, F., Scaillet, S., Molin, P., et al. (2019). Aborted propagation of the Ethiopian rift caused by linkage with the Kenyan rift. *Nature communications*, *10*(1), 1309. https://doi.org/10.1038/s41467-019-09335-2

Corti, G., Molin, P., Sembroni, A., Bastow, I. D., & Keir, D. (2018). Control of pre-rift lithospheric structure on the architecture and evolution of continental rifts: Insights from the Main Ethiopian Rift, East Africa. *Tectonics*, *37*, 477–496. https://doi.org/10.1002/2017TC004799

Cosca, M. A., Thompson, R. A., Lee, J. P., Turner, K. J., Neymarl, L. A., & Premo, W. R. (2014). $^{40}Ar/^{39}Ar$ geochronology, isotope geochemistry (Sr, Nd, Pb), and petrology of alkaline lavas near Yampa, Colorado: Migration of alkaline volcanism and evolution of the northern Rio Grande rift. *Geosphere*, *10*(2), 374–400.

Cunningham, C. G., Naeser, C. W., & Marvin, R. F. (1977). New ages for intrusive rocks in the Colorado mineral belt. *U.S. Geological Survey Open-File Report 77-573*, 7p.

Curry, M. A., Barnes, J. B., & Colgan, J. P. (2016). Testing fault growth models with low-temperature thermochronology in the northwest Basin and Range, USA. *Tectonics*, *35*, 2467–2492. https://doi.org/10.1002/2016TC004211

Dean, R. B., & Dixon, W. J. (1951). Simplified statistics for small numbers of observations. *Analytical Chemistry*, *23*(4), 636–638.

Duller, R. A., Whittaker, A. C., Swinehart, J. B., Armitage, J. J., Sinclair, H. D., Bair, A., & Allen, P. A. (2012). Abrupt landscape change post–6 Ma on the central Great Plains, USA. *Geology*, *40*(10), 871–874.

Ebinger, C. (2005). Continental break-up: The East African perspective. *Astronomy & Geophysics*, *46*(2), 2–16.

Ebinger, C., Crow, M., Rosendahl, B., Livingstone, D., & Le Fournier, J. (1984). Structural evolution of Lake Malawi. *Nature*, *308*, 627–629.

Ebinger, C. J. (1989). Tectonic development of the western branch of the East African rift System. *GSA Bulletin*, *101*(7), 885–903.

Ebinger, C. J., Karner, G. D., & Weissel, G. D. (1991). Mechanical strength of extended continental lithosphere: Constraints from the western rift system, Africa. *Tectonics*, *10*, 1239–1256.

Ebinger, C. J., van Wijk, J., & Keir, D. (2013). The time scales of continental rifting: Implications for global processes. In M. E. Bickford (Ed.), *The web of geological sciences: Advances, impacts, and interactions*, *Geological Society of America Special Paper* (Vol. 500, pp. 371–396).

Ehlers, T. A. (2005). Crustal thermal processes and the interpretation of thermochronometer data. *Reviews in Mineralogy and Geochemistry*, *58*(1), 315–350.

Epis, R. C., & Chapin, C. E. (1974). Stratigraphic nomenclature of the Thirty-nine Mile Volcanic Field, Central Colorado. *Geologic Survey Bulletin*, 1–32.

Epis, R. C., Scott, G. R., Taylor, R. B., & Chapin, C. E. (1976). Cenozoic volcanic, tectonic, and geomorphic features of Central Colorado. Studies in Colorado Field Geology, Professional Contributions Colorado School of Mines, 323–338.

Farley, K. A. (2002). (U-Th)/He dating: Techniques, calibrations, and applications. *Reviews in Mineralogy and Geochemistry*, *47*(1), 819–844.

Fletcher, A. W., Abdelsalam, M. G., Emishaw, L., Atekwana, E. A., Laó-Dávila, D. A., & Ismail, A. (2018). Lithospheric controls on the rifting of the Tanzanian craton at the Eyasi basin, eastern branch of the East African rift system. *Tectonics*, *37*, 2818–2832. https://doi.org/10.1029/2018TC005065

Flowers, R. M., Ketcham, R. A., Shuster, D. L., & Farley, K. A. (2009). Apatite (U–Th)/He thermochronometry using a radiation damage accumulation and annealing model. *Geochimica et Cosmochimica Acta*, *73*(8), 2347–2365.

Frankel, K. L., & Pazzaglia, F. J. (2006). Mountain fronts, base-level fall, and landscape evolution: Insights from the southern Rocky Mountains. In *Special Paper 398: Tectonics, Climate, and Landscape Evolution*, *Geological Society of America* (Vol. 398, pp. 419–434).

Gallagher, K. (2012). Transdimensional inverse thermal history modeling for quantitative thermochronology. *Journal of Geophysical Research*, *117*, B02408. https://doi.org/10.1029/2011JB008825

Gallagher, K., Stephenson, J., Brown, R., Holmes, C., & Fitzgerald, P. (2005). Low temperature thermochronology and modeling strategies for multiple samples 1: Vertical profiles. *Earth and Planetary Science Letters*, *237*, 193–208. https://doi.org/10.1016/J.EPSL.2005.06.025

Golombek, M. D., McGill, G. E., & Brown, L. (1983). Tectonic and geologic evolution of the Espanola Basin, Rio Grande Rift: Structure, rate of extension and relation to the state of stress in the Western United States. *Tectonophysics*, *94*, 483–507.

Grauch, V. J. S., Bauer, P. W., Drenth, B. J., & Kelson, K. I. (2017). A shifting rift—Geophysical insights into the evolution of Rio Grande rift margins and the Embudo transfer zone near Taos, New Mexico. *Geosphere*, *13*(3), 870–910.

Guenthner, W. R., Reiners, P. W., Ketcham, R. A., Nasdala, L., & Giester, G. (2013). Helium diffusion in natural zircon: Radiation damage, anisotropy, and the interpretation of zircon (U-Th)/He thermochronology. *American Journal of Science*, *313*(3), 145–198.

Hamilton, W. (1981). Plate-tectonic mechanism of Laramide deformation. *Contributions in Geology*, *19*, 87–92.

Heller, P. L., Dueker, K., & McMillan, M. E. (2003). Post-Paleozoic alluvial gravel transport as evidence of continental tilting in the US Cordillera. *Geological Society of America Bulletin*, *115*(9), 1122–1132.

House, M. A., Kelley, S. A., & Roy, M. (2003). Refining the footwall cooling history of a rift flank uplift, Rio Grande rift, New Mexico. *Tectonics*, *22*(5), 1060. https://doi.org/10.1029/2002TC001418

Hubbard, M. S., Oviatt, C. G., Kelley, S., Perkins, M. E., Hodges, K. V., & Robbins, R. (2001). Oligocene-Miocene basin formation and modification in the northern Rio Grande rift; constraints from $^{40}Ar/^{39}Ar$, fission track, and tephrochronology. *Geological Society of America Abstracts with Programs*, *33*(6), 257.

Ingersoll, R. V. (2001). Structural and stratigraphic evolution of the Rio Grande Rift, northern New Mexico and southern Colorado. *International Geology Review*, *43*(10), 867–891.

Johnson, C. M., & Thompson, R. A. (1991). Isotopic composition of Oligocene mafic volcanic rocks in the northern Rio Grande rift: Evidence of contributions of ancient intraplate and subduction magmatism to evolution of the lithosphere. *Journal of Geophysical Research*, *96*, 13,593–13,608.

Johnstone, S. A., & Colgan, J. P. (2018). Interpretation of low-temperature thermochronometer ages from tilted normal fault blocks. *Tectonics*, *37*, 3647–3667. https://doi.org/10.1029/2018TC005207

Karlstrom, K. E., & Bowring, S. A. (1988). Early Proterozoic assembly of tectonostratigraphic terranes in Southwestern North America. *The Journal of Geology*, *96*(5), 561–576.

Karlstrom, K. E., & Humphreys, E. D. (1998). Persistent influence of Proterozoic accretionary boundaries in the tectonic evolution of southwestern North America, interaction of cratonic grain and mantle modification events. *Rocky Mountain Geology*, *33*(2), 161–179.

Keir, D., Ebinger, C. J., Stuart, G. W., Daly, E., & Ayele, A. (2006). Strain accommodation by magmatism and faulting as rifting proceeds to breakup: Seismicity of the northern Ethiopian rift. *Journal of Geophysical Research*, *111*, B05314. https://doi.org/10.1029/2005JB003748

Kelley, S. (1990). Late Mesozoic to Cenozoic cooling histories of the Sangre de Cristo Mountains, Colorado and New Mexico. In Bauer, P. W., Lucas, S. G., Mawer, C. K., & McIntosh, W. C., (Eds.), *Tectonic development of the Southern Sangre de Cristo Mountains, New Mexico: New Mexico Geological Society 41st Annual Fall Field Conference Guidebook*, p. 123-132.

Kelley, S. A., & Chapin, C. E. (1995). Apatite fission-track thermochronology of Southern Rocky Mountain-Rio Grande Rift-Western High Plains Provinces. *New Mexico Geological Society Guidebook*, *46*, 87–96.

Kelley, S. A., & Chapin, C. E. (1997). Cooling histories of mountain ranges in the southern Rio Grande rift based on apatite fission-track analysis—A reconnaissance survey. *New Mexico Bureau of Mines Mineral Resources*, *19*(1), 1–14.

Kelley, S. A., Chapin, C. E., & Corrigan, A. J. (1992). Late Mesozoic to Cenozoic cooling histories of the flank of the Northern and Central Rio Grande Rift, Colorado and New Mexico. *New Mexico Bureau of Mines Mineral Resources*, *145*, 1–40.

Kelley, S. A., & Duncan, I. J. (1986). Late Cretaceous to Middle Tertiary tectonic history of the northern Rio Grande rift, New Mexico. *Journal of Geophysical Research*, *91*, 6246–6262.

Kelley, V. C. (1979). Tectonics, middle Rio Grande rift, New Mexico. *Rio Grande rift: tectonics and magmatism*, *14*, 57–70.

Kellogg, K. S. (1999). Neogene basins of the northern Rio Grande rift: Partitioning and asymmetry inherited from Laramide and older uplifts. *Tectonophysics*, *305*, 141–152.

Kellogg, K. S., Shroba, R. R., Ruleman, C. A., Bohannon, R. G., McIntosh, W. C., Premo, W. R., ... & Brandt, T. R. (2017). Geologic map of the upper Arkansas River valley region, north-central Colorado (No. 3382). US Geological Survey.

Kelson, K. I., Bauer, P. W., Unruh, J. R., & Bott, D. J. (2004). Late Quaternary characteristics of the northern Embudo fault, Taos County, New Mexico. In Brister, B. S., Bauer, P. W., Read, A. S., & Lueth, V. W. (Eds.), *New Mexico Geological Society Guidebook: 55th Field Conference, Geology of the Taos Region*, 147–157.

Kim, Y. S., & Sanderson, D. J. (2005). The relationship between displacement and length of faults: A review. *Earth-Science Reviews*, *68*(3-4), 317–334.

Kluth, C. F., & Schaftenaar, C. H. (1994). Depth and geometry of the northern Rio Grande Rift in the San Luis Basin, south-central Colorado. In G. R. Keller, & S. M. Cather (Eds.), *Basins of the Rio Grande Rift: Structure, stratigraphy and tectonic setting*, *Geological Society of America Special Paper* (Vol. 291, pp. 27–38).

Knepper, D. H. Jr. (1974). Tectonic analysis of the Rio Grande rift zone, central Colorado. [Doctoral Thesis] Colorado School of Mines, Golden, CO.

Koning, D. J., Aby, S., Grauch, V. J. S., & Zimmerer, M. J. (2016). Latest Miocene–earliest Pliocene evolution of the ancestral Rio Grande at the Española–San Luis Basin boundary, northern New Mexico. *New Mexico Geology*, *38*(2), 24–49.

Kreemer, C., Blewitt, G., & Bennett, R. A. (2010). Present-day motion and deformation of the Colorado Plateau. *Geophysical Research Letters*, *37*, L10311. https://doi.org/10.1029/2010GL043374

Landman, R., & Flowers, R. M. (2013). (U-Th)/He thermochronologic constraints on the evolution of the northern Rio Grande Rift, Gore Range, Colorado, and implications for rift propagation models. *Geosphere*, *9*(1), 170–187.
Lavecchia, A., Thieulot, C., Beekman, F., Cloetingh, S., & Clark, S. (2017). Lithosphere erosion and continental breakup: Interaction of extension, plume upwelling and melting. *Earth and Planetary Science Letters*, *467*, 89–98.
Leat, P. T., Thompson, R. N., Dickin, A. P., Morrison, M. A., & Hendry, G. L. (1989). Quaternary volcanism in northwestern Colorado: Implications for the roles of asthenosphere and lithosphere in the genesis of continental basalts. *Journal of Volcanism Geothermal Research*, *37*, 291–310.
Leat, P. T., Thompson, R. N., Morrison, M. A., Hendry, G. L., & Dickin, A. P. (1990). Geochemistry of mafic lavas in the early Rio Grande rift, Yarmony Mountain, Colorado, U.S.A. *Chemical Geology*, *81*, 23–43.
Leonard, E. M. (2002). Geomorphic and tectonic forcing of late Cenozoic warping of the Colorado piedmont. *Geology*, *30*(7), 595–598.
Leonard, E. M., Hubbard, M. S., Kelley, S. A., Evanoff, E., Siddoway, C. S., Oviatt, C. G., et al. (2002). High Plains to Rio Grande rift: Late Cenozoic evolution of central Colorado. In Geological Society of America Meeting Field Trip Guidebook*:* Geological Society of America, Boulder, Colorado, 35 p.
Levander, A., Schmandt, B., Miller, M. S., Liu, K., Karlstrom, K. E., Crow, R. S., et al. (2011). Continuing Colorado plateau uplift by delamination style convective lithospheric down-welling. *Nature*, *472*, 461–466.
Lewis, C. J., & Baldridge, W. S. (1994). Crustal extension in the Rio Grande rift, New Mexico: Half-grabens, accommodation zones, and shoulder uplifts in the Ladron Peak-Sierra Lucero area. *Geological Society of America, Special Paper*, *291*, 135–155.
Limbach, F. W. (1975). The geology of the Buena Vista area, Chaffee county, Colorado: [Doctoral Thesis]. Colorado School of Mines, Golden, Colorado, T-1692.
Lindsey, D. A., Andriessen, P. A. M., & Wardlaw, B. R. (1986). Heating, cooling, and uplift during Tertiary time, northern Sangre de Cristo Range, Colorado. *Geological Society of America Bulletin*, *97*, 1133–1143.
Lindsey, D. A., Lohnson, B. R., & Andriessen, P. A. M. (1983). Laramide and Neogene structure of the northern Sangre de Cristo Range, south-central Colorado. In J. D. Lowell (Ed.), *Rocky mountain foreland basins and uplifts*, *Rocky Mountain Association of Geology* (pp. 219–228). Denver, CO: AAPG Bulletin.
Lipman, P. W., & Mehnert, H. H. (1975). Late Cenozoic basaltic volcanism and development of the Rio Grande depression in the Southern Rocky Mountains. In Curtis, B. F. (Ed.). *Cenozoic history of the southern Rocky Mountains: Geological Society of America Memoir*, *144*, 119–154.
Liu, Y. A., Murphy, M. A., van Wijk, J., Koning, D. J., Smith, T., & Andrea, R. A. (2019). Progressive opening of the northern Rio Grande rift based on fault structure and kinematics of the Tusas-Abiquiu segment in north-central New Mexico, US. *Tectonophysics*, *753*, 15–35.
Lozinsky, R. P. (1988). Stratigraphy, sedimentology, and sand petrology of the Santa Fe Group and pre-Santa Fe Tertiary deposits in the Albuquerque basin, central New Mexico. [Doctoral Thesis], New Mexico Institute of Mining and Technology, Socorro, New Mexico.
Machette, M. N. (1988). Quaternary movement along the La Jencia fault, central New Mexico. *U.S. Geological Survey Professional Paper 1440*, 82, 2 plates.
Machette, M. N., Personious, S. F., Kelson, K. I., Haller, K. M., & Dart, R. L. (1998). Map of Quaternary faults and folds in New Mexico and adjacent areas. *USGS Open-file report 98-521*.
Mack, G. H., & Seager, W. R. (1995). Transfer zones in the southern Rio Grande rift. *Journal of the Geological Society*, *152*(3), 551–560.
Manley, C. R., Glazner, A. F., & Farmer, G. L. (2000). Timing of volcanism in the Sierra Nevada of California: Evidence for Pliocene delamination of the batholithic root? *Geology*, *28*(9), 811–814.
May, S. J., & Russell, L. R. (1994). Thickness of the syn-rift Santa Fe Group in the Albuquerque Basin and its relation to structural style. In Keller, G. R., & Cather, S. M. (Eds.). *Basins of the Rio Grande rift: Structure, stratigraphy, and tectonic setting: Geological Society of America Special Paper*, *291*, 113–124.
McCall, A. M., & Kodama, K. P. (2014). Anisotropy-based inclination correction for the Moenave Formation and Wingate Sandstone: Implications for Colorado Plateau rotation. *Frontiers in Earth Science*, *2*, 15.
McClay, K. R., Dooley, T., Whitehouse, P., & Mills, M. (2002). 4-D evolution of rift systems: Insights from scaled physical models. *AAPG bulletin*, *86*(6), 935–959.
McIntosh, W. C., & Quade J. (1995). $^{40}Ar/^{39}Ar$ geochronology of the tephra layers in the Santa Fe Group, Española Basin, New Mexico. *New Mexico Geological Society Guidebook, 46th Field Conference*, 279-287.
McMillan, M. E., Angevine, C. L., & Heller, P. L. (2002). Post depositional tilt of the Miocene-Pliocene Ogallala Group on the western Great Plains: Evidence of late Cenozoic uplift of the Rocky Mountains. *Geology*, *30*(1), 63–66.
McMillan, N. J., Dickin, A. P., & Haag, D. (2000). Evolution of magma source regions in the Rio Grande rift, southern New Mexico. *GSA Bulletin*, *112*(10), 1582–1593.
Miggins, D. P., Thompson, R. A., Pillmore, C. L., Snee, L. W., & Stern, C. R. (2002). Extension and uplift of the northern Rio Grande rift: Evidence from 40Ar/39Ar geochronology from the Sangre de Cristo Mountains, south-central Colorado and northern New Mexico. In M. A. Menzies, S. L. Klemperer, C. J. Ebinger, & J. Baker (Eds.), *Volcanic rifted margins*, *Geological Society of America Special Paper* (Vol. 362, pp. 47–64).
Miller, M. G. (1999). Active breaching of a geometric segment boundary in the Sawatch Range normal fault, Colorado, USA. *Journal of Structural Geology*, *21*, 769–776.
Minor, S.A., Caine, J.S., Ruleman, C.A., Fridrich, C.J., Chan, C.F., Brandt, T.R., et al. (2019). Geologic map of the Poncha Pass area, Chaffee, Fremont, and Saguache Counties, Colorado. *U.S. Geological Survey Scientific Investigations Map 3436*, (scale 1:24,000).
Molnar, N. E., Cruden, A. R., & Betts, P. G. (Eds) (2017). Interactions between propagating rotational rifts and linear rheological heterogeneities: Insights from three-dimensional laboratory experiments. *Tectonics*, *36*, 420–443. https://doi.org/10.1002/2016TC004447
Morgan, M. L. (2017). Colorado Earthquake Map Server: https://dnrwebmapgdev.state.co.us/CGSOnline/
Morgan, P. W., Seager, R., & Golombek, M. P. (1986). Cenozoic thermal, mechanical and tectonic evolution of the Rio Grande rift. *Journal of Geophysical Research*, *91*, 6263–6276.
Morley, C. K. (1988). Variable extension in lake Tanganyika. *Tectonics*, *7*(4), 785–801.
Morley, C. K., Nelson, R. A., Patton, T. L., & Munn, S. G. (1990). Transfer zones in the East African rift system and their relevance to hydrocarbon exploration in rifts (1). *AAPG Bulletin*, *74*(8), 1234–1253.
Muehlberger, W. R., Belcher, R. C., & Goetz, L. K. (1978). Quaternary faulting in trans-Pecos Texas. *Geology*, *6*(6), 337–340.
Muirhead, J. D., Kattenhorn, S. A., & Le Corvec, N. (2015). Varying styles of magmatic strain accommodation across the East African Rift. *Geochemistry, Geophysics, Geosystems*, *16*, 2775–2795. https://doi.org/10.1002/2015GC005918

Muirhead, J. D., Kattenhorn, S. A., Lee, H., Mana, S., Turrin, B. D., Fischer, T. P., et al. (2016). Evolution of upper crustal faulting assisted by magmatic volatile release during early-stage continental rift development in the East African Rift. *Geosphere*, *12*(6), 1670–1700. https://doi.org/10.1130/GES01375.1

Naeser, C. W., Bryant, B., Kunk, M. J., Kellogg, K., Donelick, R. A., & Perry, W. J. Jr. (2002). Tertiary cooling and tectonic history of the White River uplift, Gore Range, and western Front Range, central Colorado: Evidence from fission-track and $^{39}Ar/^{40}Ar$ ages. *Geological Society of America Special Papers*, *366*, 31–53.

Nakai, J. S., Sheehan, A. F., & Bilek, S. L. (2017). Seismicity of the Rocky Mountains and Rio Grande rift from the Earthscope Transportable Array and CREST temporary seismic networks, 2008–2010. *Journal of Geophysical Research: Solid Earth*, *122*, 2173–2192. https://doi.org/10.1002/2016JB013389

Nelson, R. A., Patton, T. L., & Morley, C. K. (1992). Rift-segment interaction and its relation to hydrocarbon exploration in continental rift systems. *American Association of Petroleum Geologists Bulletin*, *76*, 1153–1160.

New Mexico Bureau of Geology and Mineral Resources (2003). Geologic Map of New Mexico, (scale 1:500,000).

Nixon, C. W., McNeill, L. C., Bull, J. M., Bell, R. E., Gawthorpe, R. L., Henstock, T. J., et al. (2016). Rapid spatiotemporal variations in rift structure during development of the Corinth Rift, central Greece. *Tectonics*, *35*, 1225–1248. https://doi.org/10.1002/2015TC004026

Peterson, C. H. L. O. E., & Roy, M. O. U. S. U. M. I. (2005). Gravity and flexure models of the San Luis, Albuquerque, and Tularosa Basins in the Rio Grande Rift, New Mexico and southern Colorado. In *Field Conference Guide book NM Geological Society*, *56*, 105–114.

Reiners, P. W. (2005). Zircon (U-Th)/He thermochronometry. *Reviews in Mineralogy and Geochemistry*, *58*(1), 151–179.

Reiners, P. W., Farley, K. A., & Hickes, H. J. (2002). He diffusion and (U–Th)/He thermochronometry of zircon: Initial results from Fish Canyon Tuff and Gold Butte. *Tectonophysics*, *349*(1), 297–308.

Reyners, M., Eberhart-Phillips, D., & Stuart, G. (2007). The role of fluids in lower crustal earthquakes near continental rifts. *Nature*, *446*(7139), 1075–1078. https://doi.org/10.1038/nature05743

Ricketts, J. W., Karlstrom, K. E., & Kelley, S. A. (2015). Embryonic core complexes in narrow continental rifts: The importance of low-angle normal faults in the Rio Grande rift of central New Mexico. *Geosphere*, *11*(2), 425–444.

Ricketts, J. W., Kelley, S. A., Karlstrom, K. E., Schmandt, B., Donahue, M. S., & van Wijk, J. (2016). Synchronous opening of the Rio Grande rift along its entire length at 25–10 Ma supported by apatite (U-Th)/He and fission-track thermochronology, and evaluation of possible driving mechanisms. *Geological Society of America Bulletin*, *128*(3-4), 397–424.

Rowland, J. V., Baker, E., Ebinger, C. J., Keir, D., Kidane, T., Biggs, J., et al. (2007). Fault growth at a nascent slow-spreading ridge: 2005 Dabbahu rifting episode, Afar. *Geophysical Journal International*, *171*(3), 1226–1246. https://doi.org/10.1111/j.1365-246X.2007.03584.x

Rowland, J. V., Wilson, C. J., & Gravley, D. M. (2010). Spatial and temporal variations in magma-assisted rifting, Taupo Volcanic Zone, New Zealand. *Journal of Volcanology and Geothermal Research*, *190*(1-2), 89–108.

Rudzitis, S., Reid, M. R., & Blichert-Toft, J. (2016). On edge melting under the Colorado Plateau margin. *Geochemistry, Geophysics, Geosystems*, *17*, 2835–2854. https://doi.org/10.1002/2016GC006349

Russell, L. R., & Snelson, S. (1994). Structure and tectonics of the Albuquerque basin segment of the Rio Grande rift: Insights from reflection seismic data. *Geological Society of America, Special Paper*, *291*, 83–112.

Sanford, A. R., Mott, R. P., Shuleski, P. J., Rinehart, E. J., Caravella, F. J., Ward, R. M., & Wallace, T. C. (1977). Geophysical evidence for a magma body in the crust in the Vicinity of Socorro, New Mexico. In J. G. Heacock, G. V. Keller, J. E. Oliver, & G. Simmons (Eds.), *The Earth's crust* (pp. 385–403). Washington, DC: American Geophysical Union.

Savage, M. K., Silver, P. G., & Meyer, R. P. (1990). Observations of teleseismic shearwave splitting in the Basin and Range from portable and permanent stations. *Geophysical Research Letters*, *17*, 21–24.

Scott, D. H., & Trask, N. J. (1971). *Geology of the lunar crater volcanic field*. Nevada: Nye County.

Scott, G. R. (1975). Reconnaissance geologic map of the Buena Vista quadrangle, Chaffee and Park Counties, Colorado. *U.S. Geological Survey, Miscellaneous Field Studies Map MF-657* (scale 1:62,500).

Shannon, J. R. (1988). Geology of the Mount Aetna cauldron complex, Sawatch Range, Colorado. [Doctoral Thesis], Colorado School of Mines, Golden, CO.

Shaw, C. A., & Karlstrom, K. E. (1999). The Yavapai-Mazatzal crustal boundary in the Southern Rocky Mountains. *Rocky Mountain Geology*, *34*(1), 37–52.

Shirvell, C., Stockli, D. F., Axen, G. J., & Grove, M. (2009). Miocene–Pliocene exhumation along the West Salton Detachment Fault (WSDF), Southern California, from (U–Th)/He thermochronometry of Apatite and Zircon. *Tectonics*, *28*, TC2006. https://doi.org/10.1029/2007TC002172

Shuster, D. L., Flowers, R. M., & Farley, K. A. (2006). The influence of natural radiation damage on helium diffusion kinetics in apatite. *Earth and Planetary Science Letters*, *249*(3-4), 148–161.

Smith, G. A. (2004). Middle to late Cenozoic development of the Rio Grande rift and adjacent regions in northern New Mexico. In G. H. Mack, & K. A. Giles (Eds.), *The geology of New Mexico: A geologic history: New Mexico Geological Society*, *Special Publication* (Vol. 11, pp. 331–358). New Mexico: Geological Society Special Publication 11.

Stahl, T., & Niemi, N. A. (2017). Late Quaternary faulting in the Sevier Desert driven by magmatism. *Scientific reports*, *7*, 44372.

Stockli, D. F., Farley, K. A., & Dumitru, T. A. (2000). Calibration of the apatite (U-Th)/He thermochronometer on an exhumed fault block, White Mountains, California. *Geology*, *28*(11), 983–986.

Stockli, D. F., Surpless, B. E., Dumitru, T. A., & Farley, K. A. (2002). Thermochronological constraints on the timing and magnitude of Miocene and Pliocene extension in the central Wassuk Range, western Nevada. *Tectonics*, *21*(4).

Taylor, R. B. (1975). Neogene tectonism in south-central Colorado. *Geological Society of America Memoirs*, *144*, 211–226.

Tweto, O. (1979). The Rio Grande rift system in Colorado. In R. E. Reiker (Ed.), *Rio Grande rift: Tectonics and magmatism* (pp. 33–56). Washington DC: American Geophysical Union.

U.S. Geological Survey (2006). Quaternary fault and fold database for the United States, accessed February 2018 from USGS web site: http// https://earthquake.usgs.gov/hazards/qfaults/

Valentine, G. A., & Cortés, J. A. (2013). Time and space variations in magmatic and phreatomagmatic eruptive processes at Easy Chair (Lunar Crater Volcanic Field, Nevada, USA). *Bulletin of Volcanology*, *75*(9), 752.

Van Alstine, R. E. (1969). Geology and mineral deposits of the Poncha Springs NE Quadrangle, Chaffee County, Colorado. *U. S. Geological Survey Special Paper*, *626*, 1–52.

Van Alstine, R. E., & Lewis, G. E. (1960). Pliocene sediments near Salida, Chaffee County, Colorado. U.S. Geological Survey Professional Paper 400-B, B245.

van Wijk, J., Koning, D., Axen, G., Coblentz, D., Gragg, E., & Sion, B. (2018). Tectonic subsidence, geoid analysis, and the Miocene-Pliocene unconformity in the Rio Grande rift, southwestern United States: Implications for mantle upwelling as a driving force for rift opening. *Geosphere*, *14*(2), 684–709.

van Wijk, J. W., Baldridge, W. S., van Hunen, J., Goes, S., Aster, R., Coblentz, D. D., et al. (2010). Small-scale convection at the edge of the Colorado Plateau: Implications for topography, magmatism, and evolution of Proterozoic Lithosphere. *Geology*, *38*(7), 611–614.

Woodward, L. A. (1977). Rate of crustal extension across the Rio Grande rift near Albuquerque, New Mexico. *Geology*, *5*, 269–272.

Zhu, L., & Fan, M. (2018). Detrital zircon provenance record of Middle Cenozoic landscape evolution in the Southern Rockies, USA. Sedimentary Geology.

Zoback, M. L., & Thompson, G. A. (1978). Basin and range rifting in northern Nevada: Clues from a mid-Miocene rift and its subsequent offsets. *Geology*, *6*(2), 111–116.